RESEARCH ARTICLE

WILEY

Wave reflection and cut-off frequencies in coupled FE-peridynamic grids

Ilias N. Giannakeas[1] | Theodosios K. Papathanasiou[1] | Hamid Bahai[2]

[1]Department of Civil and Environmental Engineering, Brunel University London, Uxbridge, UK

[2]Department of Mechanical and Aerospace Engineering, Brunel University London, Uxbridge, UK

Correspondence
Theodosios K. Papathanasiou, Department of Civil and Environmental Engineering, Brunel University London, Uxbridge UB8 3PH, UK.
Email: theodosios.papathanasiou@brunel.ac.uk

Summary

Reflections are typically observed when pulses propagate across interfaces. Accordingly, spurious reflections might occur at the interfaces between different models used to simulate the same medium. Examples of such coupled models include classical continuum descriptions with molecular dynamics or peridynamic (PD) grids. In this work, three different coupling approaches are implemented to couple bond-based PDs with finite element (FE) solvers for solid mechanics. It is observed that incorporation of an overlapping zone, over which the coupling between FE and PD occurs, can lead to minimization of the reflected energy compared to a standard force coupling at the FE domain/PD grid interface. However, coupling with other existing methodologies, like the addition of ghost particles, achieves comparable accuracy at lower computational cost. Furthermore, the prudent selection of the discretization parameters is of pivotal importance as they control the high frequency cut-off limit. Mismatch between the cut-off frequencies of the different descriptions can lead to unrealistic results.

KEYWORDS

bond-based peridynamics, coupling, finite elements, perfectly matched layer, spurious reflections

1 | INTRODUCTION

The computational cost associated with the implementation of the peridynamic (PD) theory is an important issue for large scale analyses.[1] One way to circumvent this drawback is through the incorporation of adaptive refinement techniques near areas where higher resolution is required (eg, near loads, boundaries, crack tips) whilst reducing the number of particles away from areas with stress concentrations. Such an approach leads to a more computationally efficient model and has been analyzed by several authors, eg, Bobaru and Ha[2] and Dipasquale et al.[3]

A different approach is through coupling classical continuum elasticity (CCM) with the PD theory. It is preferred that CCM is used in areas where failure is not expected to happen, whereas PD are used to model the behaviour at the vicinity of a failure site, like crack tips, voids, inclusions, notches, etc. The solution of the underlying partial differential equation of classical elasticity is typically approximated using solvers based on the finite element (FE) method.[4] The PD equation of motion on the other hand is usually discretized using a grid of material points/particles and the solution is approximated at their location.[5,6] Because the coupling between these two solutions is commonly realised after the discretization of CCM

and PD, it is usually described in the literature as coupling FE with PD grids (see, eg, other works[7-10]). This terminology is also adopted here. Using such a coupling approach, it is envisaged to combine the computational efficiency of FE with the ability of PD to accommodate discontinuous fields and microstructural characteristics within the solution domain.[11]

The advantages of coupling a computational efficient local theory with the capabilities that are offered in finer-scale descriptions (eg, molecular dynamics) have already been identified within multiscale applications.[12] One of the challenges in the coupling methodologies arises when dynamic problems are considered. Due to model mismatch, unrealistic reflections occur when waves propagate across the domains simulated using different models. Substantial effort has been devoted to formulating a methodology that is able to effectively communicate the information between the various descriptions, with several approaches having been proposed to achieve coupling between continuum with atomistic/molecular descriptions. A recent review on this subject can be found in the work of Miller and Tadmor.[13] The coupling methods can be divided into two broad classes: (i) coupling achieved at an interface between the two descriptions of the solid and (ii) coupling being realised gradually over a finite zone, often called *overlapping zone*.[14,15] It is noted that one of the advantages of overlapping zones is that they can reduce the spurious reflections as well as allow the two models to have different levels of discretization refinement.[14,16,17] Different levels of discretization can be also achieved using interface coupling through the "*mortar method*" where Lagrange multipliers are used to implicitly impose continuity.[18,19]

Many methodologies to couple FE with PDs have also been reported. Without being exhaustive, some contributions are reported here. Liu and Hong[8] have formulated a methodology of coupling FE with PDs using coupling forces through interface elements. In the work of Seleson et al,[20] the PD and the continuum models were blended together using a force-based coupling scheme. The fundamental difference in this approach lies in the fact that the coupled scheme was derived from a single framework instead of using two models and "gluing" them together.[20] The main advantage is that ghost forces are eliminated on the interface. In the works of Kilic and Madenci[9] and Madenci and Oterkus,[21] an overlapping zone is used for the coupling of the two models taking advantage of the FE shape functions. In the work of Han and Lubineau,[22] the Arlequin method, introduced by Dhia and Rateau,[23] is used to couple FE with the nonlocal theory presented by Di Paola et al.[24] Additionally, Han and Lubineau[22] mentioned that PDs is a suitable alternative. In subsequent publications,[1,25] the same authors use the morphing strategy, a modification of the Arlequin method, to couple PDs with FE. It is noted that, in this procedure, a damage index is used to adaptively introduce PDs in areas that are susceptible to fracture. A more complete overview of methodologies to couple FE with PDs can also be found in the work of Zaccariotto et al.[7]

In most cases, solutions using coupled FE-PD are restricted to static applications. Recently, Zaccariotto et al[7] used the coupling methodology, introduced in the work of Galvanetto et al,[26] to study dynamic problems as well. Furthermore, applications were extended to 3D problems, illustrating the ability of the coupled model to tackle more complex crack front geometries. The advantage in their methodology lies in its simplicity that does not require determination of blending functions for the two models and can be easily extended to commercial software. Exploiting the computational prowess of graphic devices able to accelerate computations,[27] 3D simulations of dynamic crack propagations can become achievable. The existence of spurious reflections due to the coupling procedure was evaluated by transmitting pulses in 1D and 2D scenarios and measuring the amplitude of the reflected wave for different PD horizon values.

In this study, a more systematic analysis regarding the appearance of spurious reflections and the underlying parameters that control the accurate transmission of incident pulses across the coupling interface/zone is presented. Three different coupling methodologies are assessed to evaluate the severity of spurious reflections generated. Emphasis is given on the importance of the cut-off frequency associated with the discretized models. In Section 2, the FE and PD models, used to describe the different domains, are defined. Section 3 provides the formulation of the different coupling approaches considered as well as a description of the problem solved. In total, three approaches are presented, ie, (i) a simple FE-PD coupling using a coincident particle and a node at the interface position, (ii) coupling using additional ghost particles, and (iii) an energy coupling of the two models over an overlapping zone. In Section 4, numerical results of the time domain analyses are presented for a 1D bar. The spurious reflections appearing in each approach are compared for different model parameters. Pulses with different shapes and frequency content are also considered. The coupling approaches presented in Section 3 are also used in Section 5 to couple PD with a continuum model, allowing to perform numerical investigations in the frequency domain and compute reflection and transmission coefficients in an infinite 1D bar. The importance of carefully selecting the discretization parameters to control the model's cut-off frequency is highlighted. Based on the findings from Section 5, one of the coupling approaches is extended to 2D problems in Section 6 to simulate pulses propagating in a plate of infinite dimensions. The unrealistic near trapping of pulses in PD regions due to ineffective coupling with FE is demonstrated, indicating that energy released from, eg, crack propagation might fail to be transferred away from the source. Finally, concluding remarks are included in Section 7.

2 | DEFINITIONS

In this section, the approaches adopted to model a solid will be briefly discussed.

2.1 | Model 1 – elasticity

First, the local theory of elasticity is briefly presented. In all cases that numerical solutions are pursued, the FE method will be adopted. The problem domain is defined as Ω^{FE}. $\partial_u\Omega$ and $\partial_F\Omega$ denote the portions of the boundary $\partial\Omega$, where displacements $\boldsymbol{u}_d$ are prescribed and surface forces $\boldsymbol{F}_d$ are applied, respectively. Throughout this work, bold notation is used to denote vector fields. The problem is thus stated as follows.

Given the initial conditions $\boldsymbol{u}(\boldsymbol{x},0)$ and $\dot{\boldsymbol{u}}(\boldsymbol{x},0)$ and for $\boldsymbol{x} \in \Omega^{\text{FE}}$, $t \in [0,T]$, find $\boldsymbol{u}$ such that

$$\rho\ddot{\boldsymbol{u}} = div\boldsymbol{\sigma} + \boldsymbol{f}_d \text{ on } \Omega^{\text{FE}} \text{ with } \boldsymbol{u} = \boldsymbol{u}_d \text{ on } \partial_u\Omega \text{ and } \boldsymbol{\sigma}\cdot\boldsymbol{n} = \boldsymbol{F}_d \text{ on } \partial_F\Omega, \tag{1}$$

where $\boldsymbol{u}$ is the displacement vector, $\boldsymbol{\sigma}$ is the stress tensor, $\boldsymbol{n}$ is the outward unit vector, and $\boldsymbol{f}_d$ are the applied body forces. To enable the FE discretization of Ω^{FE}, the weak (or variational) formulation of Equation (1) is used. Then, the aforementioned problem can be rewritten as follows.

Given the initial conditions $\boldsymbol{u}(\boldsymbol{x}, 0)$ and $\dot{\boldsymbol{u}}(\boldsymbol{x},0)$, find $\boldsymbol{u}$ such that

$$\int_{\Omega^{\text{FE}}} \rho\ddot{\boldsymbol{u}}\cdot\delta\dot{\boldsymbol{u}}d\Omega + \int_{\Omega^{\text{FE}}} \boldsymbol{\varepsilon}(\boldsymbol{u}) : \boldsymbol{E} : \boldsymbol{\varepsilon}(\delta\dot{\boldsymbol{u}})\,d\Omega = \int_{\Omega^{\text{FE}}} \boldsymbol{f}_d\cdot\delta\dot{\boldsymbol{u}}d\Omega + \int_{\partial_F\Omega} \boldsymbol{F}_d\cdot\delta\dot{\boldsymbol{u}}dS \tag{2}$$

for all admissible $\delta\dot{\boldsymbol{u}}$. In addition, it is $\boldsymbol{\varepsilon}(\boldsymbol{u}) = \frac{1}{2}(\nabla\boldsymbol{u} + \nabla\boldsymbol{u}^T)$ and $\boldsymbol{E}$ is the fourth-order elastic tensor. Without loss of generality, in the following, we assume that no body forces and tractions are applied. The displacement field $\boldsymbol{u}$ is approximated by classical FE shape functions as follows:

$$\boldsymbol{u}(\boldsymbol{x}) \approx \sum_{i=1}^{N_{np}} N_i(\boldsymbol{x})\boldsymbol{u_i} = \boldsymbol{N}^T\boldsymbol{U}, \tag{3}$$

where N_{np} is the total number of mesh nodes in Ω^{FE}, $\boldsymbol{U}$ is the displacement vector at the FE nodal positions, and $N_i(\boldsymbol{x})$ are continuous piecewise polynomial base functions. The discrete form of Equation (2) can be written as follows:

$$\boldsymbol{M}\ddot{\boldsymbol{U}} + \boldsymbol{K}\boldsymbol{U} = \boldsymbol{F}, \tag{4}$$

where $\boldsymbol{F}$ is the force vector and $\boldsymbol{M}$ and $\boldsymbol{K}$ are the mass and stiffness matrices, respectively, defined as follows:

$$\boldsymbol{M} = \sum_{i=1}^{N_{en}} \int_{\Omega_i} \rho\boldsymbol{N}^T\boldsymbol{N}d\Omega, \boldsymbol{K} = \sum_{i=1}^{N_{en}} \int_{\Omega_i} \frac{d\boldsymbol{N}^T}{dx}\boldsymbol{E}\frac{d\boldsymbol{N}}{dx}d\Omega, \tag{5}$$

where N_{en} is the total number of elements and Ω_i is the element domain.

In the following sections, 1D and 2D pulse propagation problems are solved. The approximation of the solution in Ω^{FE} is carried out using two-node linear bar elements for the 1D problems and four-node linear rectangular elements for the 2D problems.

2.2 | Model 2 – bond-based peridynamics

Bond-based PD is a nonlocal theory introduced by Siling.[28] The theory is based on a partial integrodifferential equation of motion[29] that avoids the use of spatial derivatives. As such, it is suitable for applications where discontinuous displacement fields appear (eg, fracture). In the literature, the PD theory has been used to simulate a wide variety of problems.[30-33] However, its implementation leads to higher computational requirements compared to FE.

According to the PD theory, a solid body is composed of material points of infinitesimal volume dV called PD particles. Each particle interacts with other particles in its vicinity through a predefined force function $\boldsymbol{f}$.[21,28] The force function contains the material information along with a length parameter, δ. This length parameters specifies the extent of the vicinity H_x, within which a particle interacts with others. The basic aspects of the PD formulation are briefly summarised here for completeness. We denote with Ω^{PD} the domain where PD theory is used. Following the work of Bobaru et al,[34]

the PD equation of motion can be written as follows:

$$\rho\ddot{\boldsymbol{d}}(\boldsymbol{x}, t) = \int_{H_x} \boldsymbol{f}\left(\boldsymbol{d}(\boldsymbol{x}', t) - \boldsymbol{d}(\boldsymbol{x}, t), \boldsymbol{x}' - \boldsymbol{x}\right) dV_{\boldsymbol{x}'} + \boldsymbol{b}(\boldsymbol{x}, t), \tag{6}$$

where ρ is the density, $\boldsymbol{d}$ is the displacement vector, $\boldsymbol{x}$ is the position vector, $\boldsymbol{b}$ is the body force field, and $\boldsymbol{f}$ is the pairwise force function, derivable from a scalar micropotential w, ie,

$$\boldsymbol{f}(\boldsymbol{\eta}, \boldsymbol{\xi}) = \frac{\partial w(\boldsymbol{\eta}, \boldsymbol{\xi})}{\partial \boldsymbol{\eta}}, \forall \boldsymbol{\eta}, \boldsymbol{\xi}. \tag{7}$$

From the definition of bond-based PD, the pairwise forces are assumed to be collinear, equal in magnitude and opposite to satisfy linear and angular momentum,[28] ie,

$$\boldsymbol{f}(\boldsymbol{\eta}, \boldsymbol{\xi}) = -\boldsymbol{f}(-\boldsymbol{\eta}, -\boldsymbol{\xi}) \text{ and } (\boldsymbol{\eta} + \boldsymbol{\xi}) \times \boldsymbol{f}(\boldsymbol{\eta}, \boldsymbol{\xi}) = 0, \forall \boldsymbol{\eta}, \boldsymbol{\xi}, \tag{8}$$

where $\boldsymbol{\xi} = \boldsymbol{x}' - \boldsymbol{x}$ is the relative position vector and $\boldsymbol{\eta} = \boldsymbol{d}' - \boldsymbol{d}$ is the relative displacement vector.

Using the definition of a microelastic material,[5] the pairwise force function can be written in the form

$$\boldsymbol{f}(\boldsymbol{\eta}, \boldsymbol{\xi}) = k(\boldsymbol{\xi}) \frac{|\boldsymbol{\eta} + \boldsymbol{\xi}| - |\boldsymbol{\xi}|}{|\boldsymbol{\xi}|} \frac{\boldsymbol{\eta} + \boldsymbol{\xi}}{|\boldsymbol{\eta} + \boldsymbol{\xi}|} = k(\boldsymbol{\xi}) s \frac{\boldsymbol{\eta} + \boldsymbol{\xi}}{|\boldsymbol{\eta} + \boldsymbol{\xi}|}, \tag{9}$$

where s is the bond stretch and $k(\boldsymbol{\xi})$ is the bond constant. The value of the bond constant can be evaluated by equating the PD strain energy with its counterpart from classical elasticity.[32] The value of $k(\boldsymbol{\xi})$ depends only on the relative position of two particles and describes a linear force-stretch ($\boldsymbol{f} - s$) particle interaction relationship analogous to a spring idealisation. Nevertheless, the PD equation of motion describes a nonlinear system of equations. In the work of Silling,[28] a linearized version of the PD theory was also derived. The linearized force function reduces to

$$\boldsymbol{f}^{lin}(\boldsymbol{\eta}, \boldsymbol{\xi}) = C(\boldsymbol{\xi}) \cdot \boldsymbol{\eta} = \frac{k(\boldsymbol{\xi})\boldsymbol{\eta}}{|\boldsymbol{\xi}|}, \tag{10}$$

where, $C(\boldsymbol{\xi})$ is the second-order micromodulus tensor.[32] Throughout this work, the linearized definition of $\boldsymbol{f}$ is used. However, the coupling approaches presented in the following sections are extendible cases where the original formulation of $\boldsymbol{f}$ is used.

The integral of Equation (6) can be approximated numerically as a finite summation using the collocation method described in the work of Bobaru et al[32] as follows:

$$\rho\ddot{\boldsymbol{d}}_i = \sum_{j=1}^{N} \boldsymbol{f}_{i,j}(\boldsymbol{\eta}, \boldsymbol{\xi}) V_j + \boldsymbol{b}_i, \tag{11}$$

where N is the number of subdomains that are included within the horizon of the ith point, V_j is the volume of the jth collocation point, and $\boldsymbol{f}_{i,j}$ is the bond force between points i and j. A more elaborate discretization method has been proposed by Kilic and Madenci,[9] where the aforementioned discretization can be extracted as a special case. In Equation (11), either the original or the linearized definition of $\boldsymbol{f}$ can be used.

The discretized expression of the PD equation of motion requires the implementation of two correction factors. (i) A surface correction to account for cases where the horizon of a particle is limited due to geometrical boundaries; in the literature, this is often referred to as the "*skin effect.*"[35] The simple method presented in the work of Bobaru et al[32] is implemented here but more refined approaches have been suggested in the literature (see, eg, the work of Madenci and Oterkus[21]). (ii) A volume correction to account for cases where particles are only partially within the horizon of another particle. Here, the volume correction presented in the work of Liu and Honh[36] is employed.

The variation of the PD kinetic energy can be approximated through a finite summation as follows:

$$\delta W_{Kin}^{PD} = \int_{\Omega^{PD}} \rho\ddot{\boldsymbol{d}} \cdot \delta\dot{\boldsymbol{d}} d\Omega \approx \sum_{i=1}^{N} m_i \ddot{\boldsymbol{d}}_i \delta\dot{\boldsymbol{d}}_i, \tag{12}$$

where N is the number of particles in Ω^{PD}, $\delta\dot{\boldsymbol{d}}$ is the variation of the velocity, and $m_i = \rho V_i$ is the mass associated with the ith point.

The scalar micropotential w in Equation (7) represents the strain energy that is stored in a single bond and the strain energy density of a material point is calculated by summing the energies of the bonds within its horizon as[37]

$$W = \frac{1}{2} \int_{H_x} w(\boldsymbol{\eta}, \boldsymbol{\xi}) \, dV_{x\prime}, \tag{13}$$

where the factor 1/2 appears because the energy stored in the bond is distributed equally to each particle that connects. Following a similar approach as in the work of Han and Lubineau[22] and approximating the integral with a finite summation, the variation of the total potential energy in the PD domain can be approximated as follows:

$$\delta W_{Pot}^{PD} \approx \sum_{i=1}^{N} \sum_{j=1}^{N_H} \boldsymbol{f}\left(\boldsymbol{\eta}_{i,j}, \boldsymbol{\xi}_{i,j}\right) \delta \dot{\boldsymbol{d}}_i V_j V_i. \tag{14}$$

If no external forces or body forces are applied in the PD domain, the problem can be stated as follows.

Given the initial conditions $\boldsymbol{d}(\boldsymbol{x}, 0)$ and $\dot{\boldsymbol{d}}(\boldsymbol{x}, 0)$, find $\boldsymbol{d}$ such that

$$\sum_{i=1}^{N} m_i \ddot{\boldsymbol{d}}_i \delta \boldsymbol{d}_i - \sum_{i=1}^{N} \sum_{j=1}^{N_H} \boldsymbol{f}\left(\boldsymbol{\eta}_{i,j}, \boldsymbol{\xi}_{i,j}\right) \delta \dot{\boldsymbol{d}}_i V_j V_i = 0, \tag{15}$$

for every admissible $\delta \dot{\boldsymbol{d}}$. Similar derivations can be found in related works.[16,22,32] It is noted that both the original and the linearized version of PD can be extracted from Equation (15) by making the appropriate substitution of $\boldsymbol{f}$ from Equation (9) or Equation (10).

2.3 | Time integration

Time integration is very important for all transient problems. Originally, PD were formulated to study dynamic crack propagation in materials under impact or blast loading.[38] Since such phenomena are associated with small time scales and require many time discretization steps, explicit methods have been used widely for the time integration of the PD equation of motion. Among the commonly used time marching techniques are the central difference scheme, implemented in other works,[5,36,39] and the velocity-Verlet algorithm used in the work of Liu and Hong[8] and Ha and Bobaru.[40] Furthermore, time marching performed through forward and backward Euler differences was used in the work of Madenci and Oterkus.[21]

In this work, time integration is performed implementing the central difference method[41] (ie, Newmark-β with $\beta = 0$ and $\gamma = 0.5$) for both FE and PD. The displacements of the next time step $(n + 1)$ are computed through

$$\boldsymbol{U}^{n+1} = \boldsymbol{U}^n + \dot{\boldsymbol{U}}^n \Delta t + \frac{1}{2} \ddot{\boldsymbol{U}}^n \Delta t^2, \tag{16a}$$

$$\boldsymbol{d}_i^{n+1} = \boldsymbol{d}_i^n + \dot{\boldsymbol{d}}_i^n \Delta t + \frac{1}{2} \ddot{\boldsymbol{d}}_i^n \Delta t^2. \tag{16b}$$

Subsequently, next step accelerations are found using the next step displacements $\boldsymbol{U}^{n+1}$ and $\boldsymbol{d}_i^{n+1}$ from the FE and PD equations of motion. Finally, the velocities of the next step are

$$\dot{\boldsymbol{U}}^{n+1} = \dot{\boldsymbol{U}}^n + \frac{1}{2} \left(\ddot{\boldsymbol{U}}^n + \ddot{\boldsymbol{U}}^{n+1} \right) \Delta t, \tag{17a}$$

$$\dot{\boldsymbol{d}}_i^{n+1} = \dot{\boldsymbol{d}}_i^n + \frac{1}{2} \left(\ddot{\boldsymbol{d}}_i^n + \ddot{\boldsymbol{d}}_i^{n+1} \right) \Delta t. \tag{17b}$$

3 | COUPLING APPROACHES

To identify the fundamental mechanisms and phenomena associated with spurious wave reflections, a simple case of waves propagating in a 1D bar is used (Figure 1). The bar domain Ω, consists of the subdomains Ω^{FE} and Ω^{PD}, where $\Omega = \Omega^{FE} \cup \Omega^{PD}$ and $\Omega^{coupl} = \Omega^{FE} \cap \Omega^{PD}$, is the domain where FE-PD coupling takes place. In Ω^{FE}, the classical local theory of elasticity is used, and FE is implemented for the numerical approximation. In Ω^{PD}, the PD model is adopted. Both ends of the bar are contained in Ω^{FE}, whereas Ω^{PD} contains the middle part. In this setting, a propagating wave will cross both an FE-PD and a PD-FE interface. Using this approach has the additional benefit of circumventing the difficulty in PD to define boundary conditions.[7,28,42] Test cases of propagating pulses with different shapes are considered to identify the parameters (eg, PD horizon δ, effect of discretization size in each model) that are crucial. Using different cases of
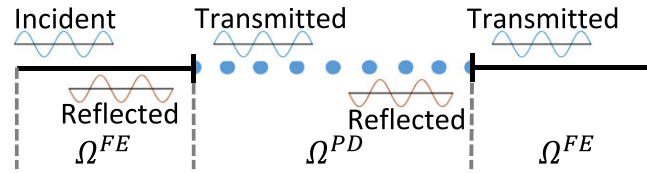
FIGURE 1 Incident and reflected wave in a 1D bar [Colour figure can be viewed at wileyonlinelibrary.com]
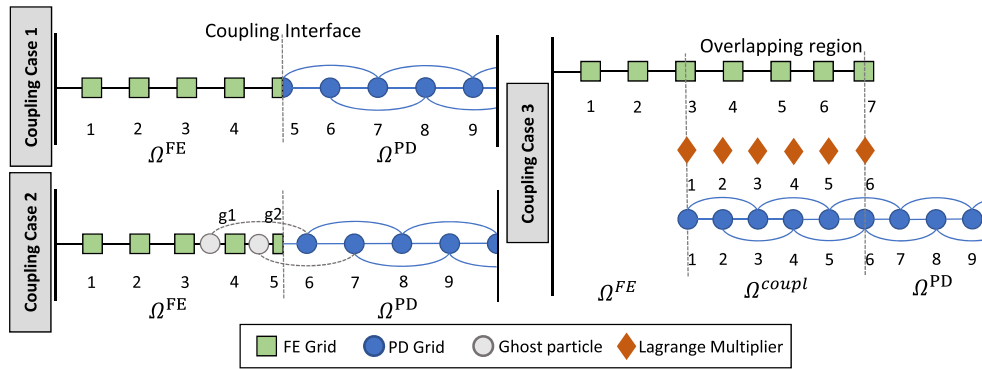
FIGURE 2 Illustration of the three approaches implemented in this study to couple finite element (FE) meshes with peridynamic (PD) grids. First two methods couple the two domains at an interface whilst the third one performs the coupling over an overlapping region [Colour figure can be viewed at wileyonlinelibrary.com]

propagating waves, the ability of each coupling methodology to accurately transfer information across the interface of the two models is studied.

A crucial point of this study is the effect of different coupling approaches on the amount of energy reflected. In total, three different coupling approaches are considered.

i. The first approach (coupling case 1 - Figure 2) involves a simple coupling between the two models. The coupling domain Ω^{coupl} consists of a single node that defines the coupling interface. Force equilibrium and continuity requirements are enforced on the interface to achieve information passing between the two models. Following this approach, it is required that an FE node and a PD particle coincide at the interface location. In this study, this is the only case where such a requirement is enforced.

ii. The second approach (coupling case 2 - Figure 2) introduces additional PD particles within the FE mesh that will be referred to as "*ghost particles*" in the subsequent sections. Recently, an approach very similar to this coupling case was presented in the works of Zaccariotto et al[7] and Galvanetto et al.[26] Similar to coupling case 1, Ω^{coupl} consists of a single node but there is no requirement that this node coincides with a PD particle. Of course, such a requirement could be applied. However, this approach will not be pursued further as realisation of this condition on general 2D and 3D interfaces can be difficult.

iii. Lastly, an energy coupling method similar to the Arlequin method (coupling case 3 - Figure 2) developed in the work of Dhia and Rateau[23] is implemented to enforce the coupling. In this case, the two models coexist in the overlapping region and Ω^{coupl} is defined over a region.

For all examples referring to a 1D bar, the value of the bond constant $k(\xi)$ is assumed to be uniform within the PD horizon $\delta = n\Delta x^{PD}$. Its value is defined as[34]

$$k(\xi) = k = \begin{cases} \frac{2E}{\delta^2 A}, & |\xi| \leq \delta \\ 0, & |\xi| > \delta. \end{cases} \tag{18}$$

3.1 | Coupling case 1

Although the first coupling case presented here is simplistic, it can be used as a reference benchmark for comparison with the other two approaches. For convenience, examples for all approaches are described using $\delta = 2\Delta x$ but the formulation remains the same for other values of δ. Assuming that the interface is at node α (eg, $\alpha = 5$ in Figure 2), to ensure continuity

between the models at the interface, it is required that

$$\boldsymbol{u}_\alpha^{\text{FE}} = \boldsymbol{d}_\alpha^{\text{PD}} = \boldsymbol{u}_\alpha. \tag{19}$$

The interface node is subjected to forces from the FE model on the left side and the PD model on the right side and the motion of node α is thus described from

$$m_\alpha \ddot{u}_\alpha = \Sigma F^{\text{FE}} + \Sigma F^{\text{PD}}, \tag{20}$$

where $m_\alpha = m_\alpha^{\text{FE}} + m_\alpha^{\text{PD}}$, m_α^{FE}, and m_α^{PD} are the mass contributions from the FE and PD model, respectively, and ΣF^{FE} and ΣF^{PD} are the total forces applied from the FE and the PD model, respectively.

Combining Equations (4), (11), (19), and (20), the final system of equations for coupling case 1 is derived. If the linearized formulation of PD is used in Ω^{PD}, it is possible to formulate the stiffness matrix of the PD bonds and write the bar response in the form $\boldsymbol{M}\ddot{\boldsymbol{U}} + \boldsymbol{K}\boldsymbol{U} = 0$. For a single FE, the stiffness matrix is given as follows:

$$K^e = \frac{EA}{l^e} \begin{bmatrix} 1 & -1 \\ -1 & 1 \end{bmatrix} = k^{\text{FE}} \begin{bmatrix} 1 & -1 \\ -1 & 1 \end{bmatrix}. \tag{21}$$

The stiffness of each PD bond is given as follows:

$$k_{i,j}^{\text{bond}} = \frac{v_{i,j}}{|\xi_{i,j}|} k(\xi) V_j V_i = \frac{2E v_{i,j} V_j V_i}{\delta^2 A |\xi_{i,j}|} = \frac{v_{i,j}}{|\xi_{i,j}|} k^{\text{PD}}, \tag{22}$$

where the volume correction $v_{i,j}$ has been included. The stiffness matrix of the bar near the interface will be computed as follows:

$$K = \begin{array}{c} \\ \alpha-2 \\ \alpha-1 \\ \alpha \\ \alpha+1 \\ \alpha+2 \\ \alpha+3 \end{array} \begin{bmatrix} \ddots & & & & & & \\ & 2k^{\text{FE}} & -k^{\text{FE}} & 0 & 0 & 0 & 0 \\ & -k^{\text{FE}} & 2k^{\text{FE}} & -k^{\text{FE}} & 0 & 0 & 0 \\ & 0 & -k^{\text{FE}} & k^{\text{FE}}+1.25k^{\text{PD}} & -k^{\text{PD}} & -0.25k^{\text{PD}} & 0 \\ & 0 & 0 & -k^{\text{PD}} & 2.25k^{\text{PD}} & -k^{\text{PD}} & -0.25k^{\text{PD}} \\ & 0 & 0 & -0.25k^{\text{PD}} & -k^{\text{PD}} & 2.5k^{\text{PD}} & -k^{\text{PD}} \\ & 0 & 0 & 0 & -0.25k^{\text{PD}} & -k^{\text{PD}} & 2.5k^{\text{PD}} \\ & & & & & & \ddots \end{bmatrix}. \tag{23}$$

with column headers $\alpha-2 \quad \alpha-1 \quad \alpha \quad \alpha+1 \quad \alpha+2 \quad \alpha+3$

Stiffness contributions from both the PD and the FE domain appear at the interface position (node 5). Furthermore, as also stated in the works of Zaccariotto et al,[7,10] when such couplings are enforced, the bandwidth of the final stiffness matrix changes due to the nonlocal nature of PD.

3.2 | Coupling case 2

In the second coupling case, ghost particles are inserted within the FE domain (Figure 2). This approach is very similar to the coupling approach presented in the aforementioned works.[7,10] The number of ghost particles is such that the PD horizon of the first particle in the PD model is not interrupted. Continuity between the two models is enforced by interpolating the nodal displacements of the FE model at the positions of the ghost particles using the FE shape functions. Hence, for $\boldsymbol{x} \in \Omega^{\text{FE}}$,

$$\boldsymbol{d} = \boldsymbol{N}^T \boldsymbol{U}. \tag{24}$$

The introduction of ghost particles does not imply that coincident FE nodes and PD particles on the interface. The forces acting on the interface from the PD model are computed by considering the forces of each individual bond that crosses the coupling interface. Denoting with $\boldsymbol{f}_{i,j}$ the force per unit volume squared particle i exerts on particle j, then the motion of the interface node is described by

$$m_\alpha \ddot{u}_\alpha = \left(k^{\text{FE}} u_\alpha - k^{\text{FE}} u_{\alpha-1} \right) + \boldsymbol{f}_{(\alpha+1),(g1)} V_{\alpha+1} V_{g1} + \boldsymbol{f}_{(\alpha+1),(g2)} V_{\alpha+1} V_{g2} + \boldsymbol{f}_{(\alpha+2),(g2)} V_{\alpha+2} V_{g2}. \tag{25}$$

Combining these time equations (4), (11), (24), and (25), the final system of equations for the second coupling case is formed. Again, using the linearized PD formulation, it is possible to construct the stiffness matrix of the system. Using the numbering in Figure 2, the displacements of the ghost particles can be written in terms of the interpolated nodal displacements as follows:

$$d_{g1} = N_{\alpha-2} u_{\alpha-2} + N_{\alpha-1} u_{\alpha-1} \text{ and } d_{g2} = N_{\alpha-1} u_{\alpha-1} + N_\alpha u_\alpha. \tag{26}$$

Using the definition of the bond stiffness in Equation (22) and combining Equations (25) and (26), the forces acting on the interface node are

$$
m_\alpha \ddot{u}_\alpha = 0.25 k^{\mathrm{PD}} N_{\alpha-2} u_{\alpha-2} - \left(k^{\mathrm{FE}} - 1.5 k^{\mathrm{PD}} N_{\alpha-1} \right) u_{\alpha-1} + \left(k^{\mathrm{FE}} + 1.25 k^{\mathrm{PD}} N_\alpha \right) u_\alpha \\
- 1.25 k^{\mathrm{PD}} d_{\alpha+1} - 0.25 k^{\mathrm{PD}} d_{\alpha+2}
$$
(27)

and the stiffness matrix becomes

$$
K = \begin{array}{c} \\ \alpha-2 \\ \alpha-1 \\ \alpha \\ \alpha+1 \\ \alpha+2 \\ \alpha+3 \end{array}
\begin{bmatrix}
\ddots & & & & & & \\
 & 2k^{\mathrm{FE}} & -k^{\mathrm{FE}} & & & & \\
 & -k^{\mathrm{FE}} & 2k^{\mathrm{FE}} & -k^{\mathrm{FE}} & & & \\
 & 0.25 k^{\mathrm{PD}} N_3 & -k^{\mathrm{FE}} + 1.5 k^{\mathrm{PD}} N_4 & k^{\mathrm{FE}} + 1.25 k^{\mathrm{PD}} N_5 & -1.25 k^{\mathrm{PD}} & -0.25 k^{\mathrm{PD}} & \\
 & -0.25 k^{\mathrm{PD}} N_3 & -1.25 k^{\mathrm{PD}} N_4 & -k^{\mathrm{PD}} N_5 & 2.5 k^{\mathrm{PD}} & -k^{\mathrm{PD}} & -0.25 k^{\mathrm{PD}} \\
 & & -0.25 k^{\mathrm{PD}} N_4 & -0.25 k^{\mathrm{PD}} N_5 & -k^{\mathrm{PD}} & 2.5 k^{\mathrm{PD}} & -k^{\mathrm{PD}} \\
 & & & & -0.25 k^{\mathrm{PD}} & -k^{\mathrm{PD}} & 2.5 k^{\mathrm{PD}} \\
 & & & & & & \ddots
\end{bmatrix}.
$$
(28)

with column labels $\alpha-2$, $\alpha-1$, α, $\alpha+1$, $\alpha+2$, $\alpha+3$.

Comparing the stiffness matrices of the first two coupling approaches, it is obvious that the nonlocality of PD has also been transferred to the interface node, whereas the horizon of the particles near the interface is not interrupted. It is noted that the stiffness matrix in Equation (28) is valid only for when the PD horizon is $\delta = 2 \Delta x^{\mathrm{PD}}$ and the ghost particles $g1$ and $g2$ lie between nodes $(\alpha-2, \alpha-1)$ and $(\alpha-1, \alpha)$, respectively. Of course, similar expressions can be derived for other values of the horizon and ghost particle location.

3.3 | Coupling case 3

In the third case, coupling is not realised at a single point but occurs along an overlapping region Ω^{coupl}, where the two models coexist (Figure 2). Coupling between the two domains is enforced in a weak sense through the implementation of Lagrange multipliers. The methodology considered is the one used by Aubertin et al,[16] for continuum to discrete coupling. Similar approaches include the Arlequin method[23] and the bridging domain method.[43] In the work of Aubertin et al,[16] FE were coupled with molecular dynamics. Here, the methodology presented in the aforementioned work[16] is adopted with the difference that the PD theory has been used instead of molecular dynamics.

Coupling in the overlapping region is achieved by introducing a coupling operator that will compare the velocities of the two models. Other coupling operators have been proposed in the literature as well. They enforce the coupling by considering the displacement fields (termed L^2 coupling) or the displacement field and its spatial derivatives (termed H^1 coupling). The interested reader can refer to the works of Dhia and Rateau[23] and Guidault and Belytschko[44] and the references therein for more information. Following the work of Aubertin et al,[16] a "*mediator space*" $\mathcal{M}$ is introduced where the velocities are projected, such that the velocity field is now defined only on discrete points that belong to a subset of Ω^{PD}. The velocities are projected on $\mathcal{M}$ using a suitable projection operator Π, a scalar product p, and Lagrange multipliers λ, such that

$$
\forall \delta\lambda \in \mathcal{M}, p\left(\delta\lambda, \Pi\dot{u} - \Pi\dot{d} \right) = 0.
$$
(29)

Similar to the case of molecular dynamics,[16] the discrete nature of PD implies that Lagrange multipliers are defined at the location of PD particles in the overlapping region. The final coupled system can be written as follows.

Given the initial conditions $u(x,0)$, $\dot{u}(x,0)$, $d(x,0)$, and $\dot{d}(x,0)$, find u and d such that

$$
\int_{\Omega^{\mathrm{FE}}} a^{\mathrm{FE}}(x) \rho \ddot{u} \cdot \delta\dot{u} d\Omega + \int_{\Omega^{\mathrm{FE}}} a^{\mathrm{FE}}(x) \varepsilon(u) : E : \varepsilon(\delta\dot{u}) \, d\Omega + p\left(\lambda, \Pi\delta\dot{u} \right) = 0
$$
(30a)

$$
\sum_{i=1}^{N} a^{\mathrm{PD}}(x) m_i \ddot{d}_i \delta\dot{d}_i - \sum_{i=1}^{N} \sum_{j=1}^{N_H} a^{\mathrm{PD}}(x) f\left(\eta_{i,j}, \xi_{i,j} \right) \delta\dot{d}_i V_j V_i - p\left(\lambda, \Pi\delta\dot{d} \right) = 0
$$
(30b)

$$
p\left(\delta\lambda, \Pi\dot{u} - \Pi\dot{d} \right) = 0,
$$
(30c)

for all admissible $\delta\dot{u}$, $\delta\dot{d}$, $\delta\lambda$, where the functions $a^{\mathrm{FE}}(x)$ and $a^{\mathrm{PD}}(x)$ define a partition of unity in the problem domain with $a^{\mathrm{FE}}(x) + a^{\mathrm{PD}}(x) = 1$. This is to ensure conservation of energy across the overlapping domain as they distribute the energy
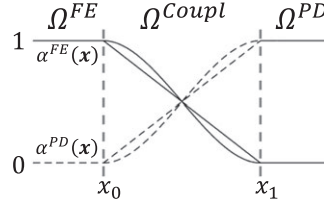
FIGURE 3 Blending functions $a^{\text{FE}}(\boldsymbol{x})$ and $a^{\text{PD}}(\boldsymbol{x})$

between the two descriptions. In many cases, these functions are called blending functions.[14] They can be defined (using the partition of unity property) through

$$a^{\text{FE}}(\boldsymbol{x}) = \begin{cases} 1, & \boldsymbol{x} \in \Omega^{\text{FE}} \\ h(\boldsymbol{x}), & \boldsymbol{x} \in \Omega^{\text{coupl}} \\ 0, & \boldsymbol{x} \in \Omega^{\text{PD}}. \end{cases} \tag{31}$$

Selection of the appropriate function $h(\boldsymbol{x})$ to distribute the energies is not straightforward and can be case dependent.[7] In the works of Guidault and Belytschko[44] and Bauman et al,[45] it was demonstrated that, when the L^2 coupling is implemented in the Arlequin method, which is very similar to the coupling implemented here, selection of Heaviside functions to distribute the energy can lead to ill-posed problems. To avoid this, continuous functions were selected to define the energy distribution (Figure 3). Two cases are used for comparison, ie, (i) a linear function with $h(\boldsymbol{x}) = \frac{x_1 - x}{x_1 - x_0}$ and (ii) a cubic function with $h(\boldsymbol{x}) = 1 - 3\left(\frac{x - x_0}{x_1 - x_0}\right)^2 + 2\left(\frac{x - x_0}{x_1 - x_0}\right)^3$.

After discretization of Equation (30) and using matrix notation, we arrive at

$$\boldsymbol{a}^{\text{FE}}\boldsymbol{M}\ddot{\boldsymbol{U}} + \boldsymbol{a}^{\text{FE}}\boldsymbol{K}\boldsymbol{U} + \boldsymbol{C}^{\text{FE}}\boldsymbol{\Lambda} = 0, \tag{32a}$$

$$\boldsymbol{a}^{\text{PD}}\boldsymbol{M}\ddot{\boldsymbol{d}} - \boldsymbol{a}^{\text{PD}}\boldsymbol{f}^{\text{PD}} - \boldsymbol{C}^{\text{PD}}\boldsymbol{\Lambda} = 0, \tag{32b}$$

$$\boldsymbol{C}^{\text{FE}}\dot{\boldsymbol{U}} - \boldsymbol{C}^{\text{PD}}\dot{\boldsymbol{d}} = 0, \tag{32c}$$

where $\boldsymbol{C}^{\text{FE}}$ and $\boldsymbol{C}^{\text{PD}}$ are the coupling matrices of the FE and PD, respectively, and $\boldsymbol{a}^{\text{FE}}$ and $\boldsymbol{a}^{\text{PD}}$ are diagonal weighting matrices. The FE velocities $\dot{\boldsymbol{U}}$ are projected on the mediator space $\mathcal{M}$ and then interpolated on the location of the PD particles in the overlapping region through the FE shape functions. Matrix $\boldsymbol{C}^{\text{FE}}$ contains the shape function values that define this interpolation. $\boldsymbol{C}^{\text{PD}}$ is a scalar Boolean matrix associating each Lagrange multiplier with a PD particle.

For the time integration of the third coupling approach, the predictor-corrector procedure presented in the work of Aubertin et al[16] is adopted. It has been shown that this procedure can further reduce the developing of spurious reflections. According to this procedure, each model is first solved individually, disregarding the coupling terms, and then the velocities and accelerations are updated in the overlapping domain using the Lagrange multipliers. The procedure proposed is briefly presented here.

First, the next step displacements $\boldsymbol{U}^{n+1}$ and $\boldsymbol{d}^{n+1}$ are calculated using Equations (16a) and (16b). Then, a prediction of the next step accelerations $\ddot{\boldsymbol{U}}^{n+1,*}$ and $\ddot{\boldsymbol{d}}^{n+1,*}$ is made as follows:

$$\ddot{\boldsymbol{U}}^{n+1,*} = -\boldsymbol{M}^{-1}\boldsymbol{a}^{\text{FE}-1}\boldsymbol{a}^{\text{FE}}\boldsymbol{K}\boldsymbol{U}^{n+1} = -\boldsymbol{M}^{-1}\boldsymbol{K}\boldsymbol{U}^{n+1} \text{ and } \ddot{\boldsymbol{d}}^{n+1,*} = \boldsymbol{m}^{-1}\boldsymbol{a}^{\text{PD}-1}\boldsymbol{a}^{\text{PD}}\boldsymbol{f}^{\text{PD}} = \boldsymbol{m}^{-1}\boldsymbol{f}^{\text{PD}}. \tag{33}$$

Using the predicted accelerations, a prediction of the next step $\dot{\boldsymbol{U}}^{n+1,*}$ and $\dot{\boldsymbol{d}}^{n+1,*}$ velocities is made using Equations (17a) and (17b). Following the work of Aubertin et al,[16] the Lagrange multipliers are computed using the predicted velocities as follows:

$$\boldsymbol{\Lambda}^{n+1} = \boldsymbol{A}^{-1}\boldsymbol{B}^{n+1}, \tag{34}$$

with $\boldsymbol{A} = \frac{\Delta t}{2}\left(\boldsymbol{C}^{\text{FE}T}\boldsymbol{M}^{-1}\boldsymbol{a}^{\text{FE}-1}\boldsymbol{C}^{\text{FE}} + \boldsymbol{C}^{\text{PD}T}\boldsymbol{m}^{-1}\boldsymbol{a}^{\text{PD}-1}\boldsymbol{C}^{\text{PD}}\right)$ and $\boldsymbol{B}^{n+1} = \boldsymbol{C}^{\text{FE}T}\dot{\boldsymbol{U}}^{n+1,*} - \boldsymbol{C}^{\text{PD}T}\dot{\boldsymbol{d}}^{n+1,*}$. Using the Lagrange multipliers calculated from Equation (34), the velocities are adjusted as follows:

$$\dot{\boldsymbol{U}}^{n+1} = \dot{\boldsymbol{U}}^{n+1,*} - \frac{1}{2}\boldsymbol{M}^{-1}\boldsymbol{a}^{\text{FE}-1}\boldsymbol{C}^{\text{FE}}\boldsymbol{\Lambda}^{n+1} \text{ and } \dot{\boldsymbol{d}}^{n+1} = \dot{\boldsymbol{d}}^{n+1,*} + \frac{1}{2}\boldsymbol{m}^{-1}\boldsymbol{a}^{\text{PD}-1}\boldsymbol{C}^{\text{PD}}\boldsymbol{\Lambda}^{n+1}, \tag{35}$$

and the accelerations as follows:

$$\ddot{\boldsymbol{U}}^{n+1} = \ddot{\boldsymbol{U}}^{n+1,*} - \boldsymbol{M}^{-1}\boldsymbol{a}^{\text{FE}-1}\boldsymbol{C}^{\text{FE}}\boldsymbol{\Lambda}^{n+1} \text{ and } \ddot{\boldsymbol{d}}^{n+1} = \ddot{\boldsymbol{d}}^{n+1,*} + \boldsymbol{m}^{-1}\boldsymbol{a}^{\text{PD}-1}\boldsymbol{C}^{\text{PD}}\boldsymbol{\Lambda}^{n+1}. \tag{36}$$

4 | NUMERICAL RESULTS

4.1 | Time-domain analyses

Using the three coupling approaches presented, wave propagation test cases are simulated numerically for the 1D bar illustrated in Figure 1. It is assumed that Young's modulus of the bar is $E = 200$ GPa, the cross-sectional area is $A = 10^{-6}$ m^2, the density is $\rho = 7850$ kg/m^3, and the total length is $l = 1.2$ m. The bar is divided into three equal parts with the middle one being modelled using the PD theory and the other two with FEs. When the third coupling case is used, the PD domain is extended within the FE domain to create the overlapping region.

Test cases with different pulse shapes are carried out. The displacement of the node at the free end of the bar is prescribed to simulate a rightward travelling incident wave. Incident pulses with two different shapes are used: a gaussian with $\boldsymbol{u}(0, t) = a_1 e^{-\frac{1}{2}\left(\frac{t-a_2}{a_3}\right)^2}$ and a modulated pulse with $\boldsymbol{u}(0, t) = \frac{a_1}{2}\sin(2\pi f_1 t) - \frac{a_1}{2}\sin(2\pi f_2 t)$. The following parameters are selected for the pulses: $a_2 = 4 \times 10^{-6}$, $a_3 = 1 \times 10^{-6}$, $f_1 = 5 \times 10^5$ Hz, and $f_2 = 5.25 \times 10^5$ Hz. In both cases, the amplitude of the pulse is $a_1 = 10^{-4}$ m. The frequency content of each pulse shape is illustrated in Figure 4.

Coupling case 1 is used first to connect FE with nonlinear PD. Both models have identical discretization lengths $\Delta x^{FE} = \Delta x^{PD} = 2 \times 10^{-4}$ m and the PD horizon is $\delta = 3\Delta x^{PD}$. A time step $\Delta t = 10^{-8}$ s is used and the duration of the analysis is $t_{tot} = 2.3 \times 10^{-4}$ s. The duration of the analysis was selected as such that travelling pulses do not reach the ends of the bar to avoid boundary reflections. In Figure 5, the spurious reflections that appear every time the pulse crosses an interface
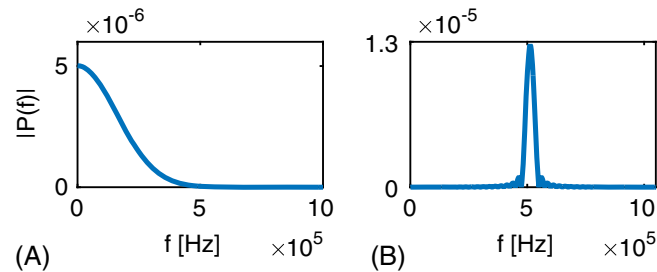
FIGURE 4 Frequency content of the (A) Gaussian and (B) modulated incident pulses [Colour figure can be viewed at wileyonlinelibrary.com]
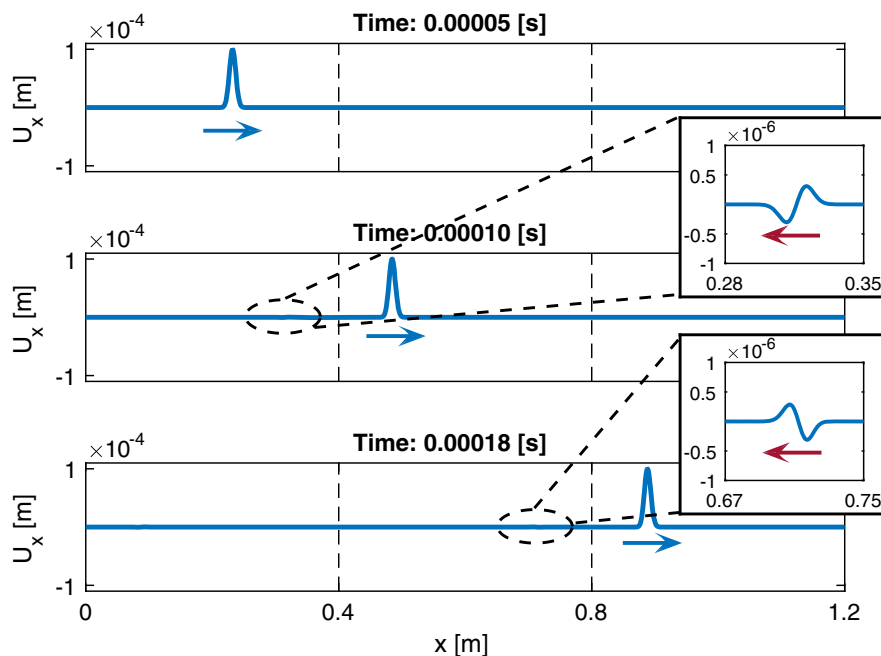
FIGURE 5 Spurious reflections using the first coupling approach to connect finite element with nonlinear peridynamics. Vertical dashed lines indicate the interface positions [Colour figure can be viewed at wileyonlinelibrary.com]
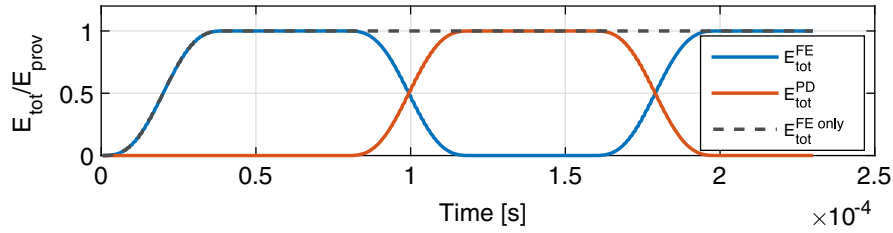
FIGURE 6   Energy transfer between the finite element and the peridynamic domain using the second coupling case and the modulated incident pulse [Colour figure can be viewed at wileyonlinelibrary.com]
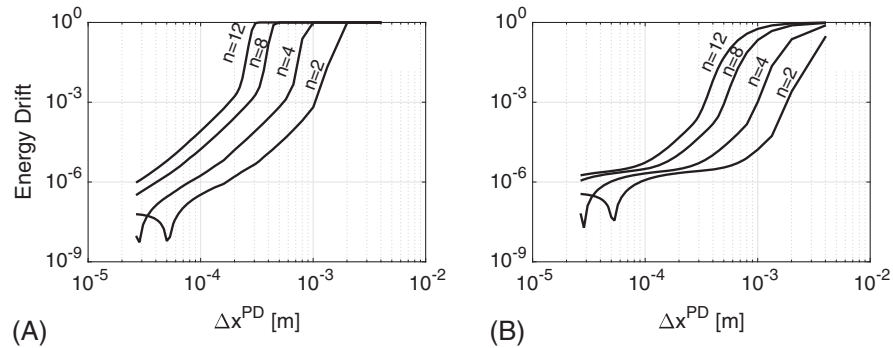
FIGURE 7   Energy drift using the second coupling case for (A) the modulated and (B) the gaussian incident pulse and for peridynamic horizon $\delta = n \Delta x^{\text{PD}}$ (the horizontal axis in log scale)

(dashed line) are illustrated. Even with a simple approach like this, it is possible to achieve information passing between FE-PD and PD-FE interfaces given that a very fine discretization is used. For the particular selection of model parameters, the amplitude of the reflected wave is approximately 3×10^{-7} m. As it will be shown later, the accuracy of this coupling deteriorates very fast as the discretization becomes coarser and this approach will only be used for comparison purposes.

To better quantify and compare the accuracy of each coupling case, the total energy within each domain is computed. As the pulse propagates through the bar, energy is transferred from the FE domain (E_{tot}^{FE}) to the PD domain (E_{tot}^{PD}) and finally back to the FE domain. Figure 6 illustrates the energy transferring between the domains using now the second coupling case with a modulated incident pulse as an example. The pulse crosses the FE-PD interface at $t = 1.19 \times 10^{-4}$ s and the energy is transferred from the FE to the PD domain. At $t = 2.03 \times 10^{-4}$ s, the pulse crosses the PD-FE interface and the energy is transferred back to the FE domain. For comparison, the total energy in an equivalent FE only model is also plotted with dashed line.

If the coupling is adequately accurate, the spurious reflections generated should be minimal and all of the energy should be transferred back to the FE domain. The accuracy of the coupling method is tested by comparing the amount of energy that was transferred to the right-hand side FE model compared to the initially provided energy. The percent error between the two energies (energy drift) is used in the following as a measure of accuracy.

Figure 7 depicts the energy drift when the second coupling case is used for different values of the PD horizon δ and discretization length Δx^{PD} for both the modulated and the Gaussian incident pulses. As δ increases, much finer grids are required to achieve comparable accuracy. It is noted that, for macroscale problems, the horizon is typically set to $\delta = 3\Delta x^{\text{PD}}$, as higher values can induce excessive dispersion and increase the required computational time, whereas lower values will lead to grid dependent crack paths.[5,21,46]

As Δx^{PD} and δ increases, total reflection of the incident wave is observed (energy drift $= 1$ in Figure 7). This is attributed to the cut-off frequency of the discrete PD model being well below the frequency content of the pulse. In such cases, the pulse never enters the PD domain and is reflected back to the FE domain. The parameters Δx^{PD} and δ are of outmost importance as they control the model's cut-off frequency.

When the third coupling case is implemented, two additional parameters need to be taken into consideration, namely, the overlapping length l^{coupl} and the choice of blending function $h(\boldsymbol{x})$ implemented within the formulation. In the work of Aubertin et al,[16] numerical tests were carried out using a linear blending function. Here, a cubic blending function is also

used. In the works of Guidault and Belytschko[44] and Bauman et al,[45] a more detailed analysis on the selection of blending functions can be found for the Arlequin method. The problem parameters are the same as before and the number of Lagrange multipliers in the coupling region is the same as the corresponding PD particles.

Using the original PD formulation and the modulated pulse, a parametric investigation is performed for different values of Δx^{PD}, δ, and l^{coupl}. In Figure 8, waterfall plots of the resulting energy drift are presented. In all cases, the conditions for total wave reflection remain unaffected by the choice of blending function and l^{coupl}. However, higher values of l^{coupl} can improve the accuracy of the coupling. Furthermore, by implementing a cubic blending function instead of a linear in the formulation, the accuracy of the coupling is improved for the same values of Δx^{PD}, δ, and l^{coupl}. This is intuitively expected since the transition is smoother in the second case. Increasing the value of l^{coupl} increases the computational cost of the method as additional PD particles and Lagrange multipliers are introduced. For the cases considered, an overlapping length of approximately $l^{coupl} = 0.01$ m seems a fair compromise between accuracy and computational cost.

Using $l^{coupl} = 0.01$ m and a cubic blending function, the energy drift is also computed for the Gaussian pulse and the results are plotted in Figure 9. Comparing Figure 7 and Figure 9, both coupling approaches exhibit total wave reflection under the same conditions, indicating that the cut-off frequency is not affected by the coupling strategy adopted. In both
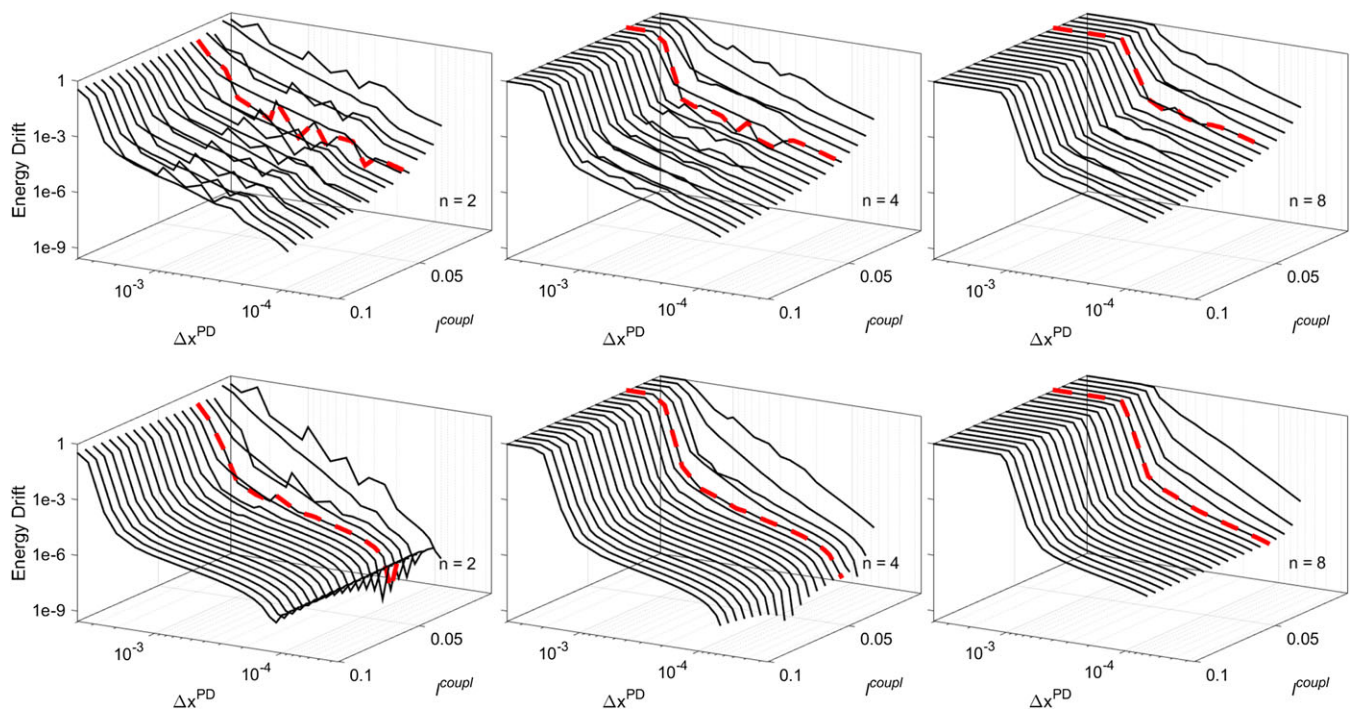
FIGURE 8 Energy drift waterfall plots using the third coupling case for a modulated pulse. The top row corresponds to results using the cubic blending function whilst the bottom to the linear. The dashed (red) line indicates the case of $l^{coupl} = 0.01$ m. The peridynamic horizon is given as $\delta = n\Delta x^{PD}$ (Δx^{PD} axis in log scale) [Colour figure can be viewed at wileyonlinelibrary.com]
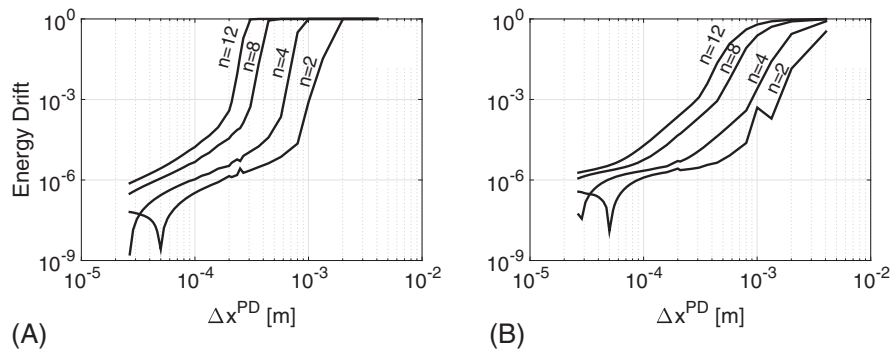
FIGURE 9 Energy drift using the third coupling case with cubic blending function and $l^{coupl} = 0.01$ m for (A) the modulated and (B) the gaussian incident pulse with peridynamic horizon $\delta = n\Delta x^{PD}$ (the horizontal axis in log scale)

cases, the higher frequency content of the modulated pulse requires refinement of the PD domain to ensure transmission. Furthermore, the accuracy achieved is comparable between the two approaches for the specific choice of parameters. If the linear blending was implemented further refinement would be necessary.

To make this investigation more general, it is of interest to continue the analysis in the frequency domain. To this end, in the next section, the linearized PD theory is coupled with a conntinuum instead of an FE approximation. Furthermore, a brief derrivation of the PD dispersion curve from the discretized equation of motion is presented as it provides insights on the cut-off frequency and its dependence on Δx^{PD} and δ that is pivotal in minimizing the spurious reflections.

5 | REFLECTION-TRANSMISSION IN A 1D CONTINUUM-PD BAR

5.1 | Dispersion curve for bond-based PD

According to the theory of elasticity, the phase velocity of a travelling wave is independent of its angular frequency ω and wavenumber κ, leading to a linear relation between ω and κ. In discretized systems however, this relation is nonlinear. Along the interface of two models with different dispersion relationships, spurious reflections occur as the incident wave travels with different speeds in each domain.[47] In PD, waves of higher frequency will travel slower than lower frequency waves. This effect needs to be taken into consideration when coupling domains that are described by different models. Additionally, discrete models exhibit a cut-off frequency that can lead to full reflection of the incident pulse. In the works of Silling et al[28,48] and Dayal,[49] the PD dispersion curve was extracted by substituting solutions with the form $\boldsymbol{u} = Ue^{i(\kappa x - \omega t)}$ into the linearized PD equation of motion and solving the resulting integral in the eigenvalue problem. In the work of Mikata,[50] the dispersion relation was derived for different micromoduli, whereas, in the work of Diyaroglu et al,[51] they are given for PD beams and plates. The dispersive characteristic of the PD theory can be also used to match the experimentally observed dispersion, as presented in the work of Butt et al.[52]

Considering a bar of infinite length and using the idealisation that the bar consists of a repeating series of masses and springs, the dispersion curve of linearized PD is derived after substitution of Equation (10) in the discretized equation of motion (11). If each particle interacts only with those that is in direct contact with $\delta = \Delta x$ and Δx is uniform, then the equation of motion for a particle becomes

$$\ddot{\boldsymbol{u}}_n = c^2 \frac{\boldsymbol{u}_{n-1} - 2\boldsymbol{u}_n + \boldsymbol{u}_{n+1}}{\Delta x^2}, \tag{37}$$

where the volume correction is also included. When $\boldsymbol{u} = Ue^{i(\omega t + \kappa x)}$, the following relationship is extracted:

$$\omega = \frac{2}{\delta}\sqrt{\frac{E}{\rho}} \sin\left(\frac{\kappa \Delta x}{2}\right). \tag{38}$$

In the limit when $\kappa \Delta x$ is very small, we can use the approximation $\sin(\kappa \Delta x/2) = \kappa \Delta x/2$ and Equation (38) leads to $\omega/\kappa \approx c$. Thus, the PD dispersion relation approximates the one extracted from the local theory of elasticity. This observation has already been described in the work of Silling.[28] Following the same procedure, the dispersion relation for various horizon lengths can be derived. As a general case, with $\delta = n\Delta x$, the dispersion relation can be written as follows:

$$\omega = \frac{2}{n\Delta x}\sqrt{\frac{E}{\rho}} \sin\left(\frac{\kappa \Delta x}{2}\right) G_n\left(\frac{\kappa \Delta x}{2}\right), \tag{39}$$

where $G_n(x)$ is a function whose expression depends on the value of the PD horizon. Expressions for $G_n(x)$ are given in Table 1, for $n = \delta/\Delta x = 1, 2, 3$, and 4. As expected, for $\kappa \Delta x \to 0$, then $G_n(x) \to n$ and Equation (39) reduces to the dispersion relationship obtained from classical elasticity.

TABLE 1 Table of expressions for $G_n(x)$

n	$G_n(x)$
1	1
2	$\sqrt{2\cos(x) + 2}$
3	$\sqrt{\frac{32}{6}\sin^4(x) - 8\sin^2(x) + 4\cos^2(x) + 5}$
4	$\sqrt{4\cos^2(x)\cos^2(2x) + \frac{32}{3}\sin^4(x) - 16\sin^2\left(\frac{x}{3}\right) + 4\cos^2(x) + 8}$
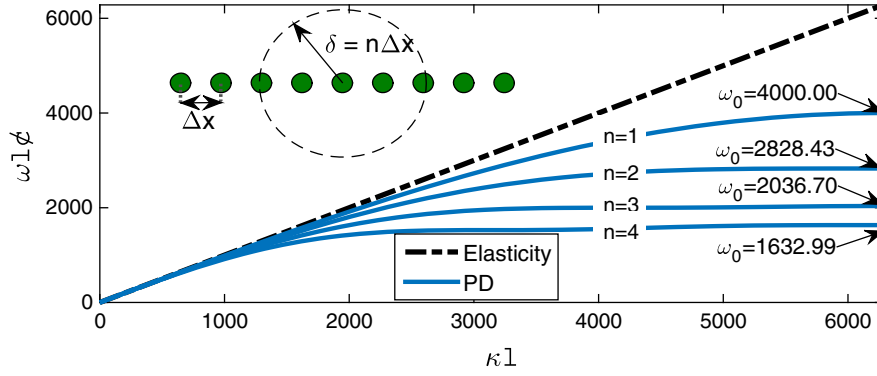
FIGURE 10 Comparison of dispersion curves between elasticity and peridynamics with $\delta = n\Delta x$. PD, peridynamic [Colour figure can be viewed at wileyonlinelibrary.com]

A comparison between the dispersion relation for different δ using Equation (39) is illustrated in Figure 10. In the same figure, the linear elasticity case has been included. It is noted that, when the value of the PD horizon is $\delta = \Delta x$, the relationship coincides with that for a two-node linear FE. The figure is plotted for wave numbers $\kappa \in (0, \pi/\Delta x)$ representing only the positive half of the first Brillouin zone. The parameters assumed are $E = 200$ GPa, $\rho = 7850$ kg/m^3, $\Delta x = 2 \times 10^{-4}$ m, and $l = 0.4$ m. An important feature for this study is that the PD cut-off frequency depends not only on the discretization length Δx but also on the value of the horizon δ. In Figure 10, the angular frequencies ω_0, which define the cut-off frequency, are indicated for each value of δ. Values have been nondimensionalised with respect to $c = \sqrt{E/\rho}$ and l.

5.2 | Continuum-PD coupling and frequency domain analyses

Coupling of linearized PD theory with continuum allows the use of frequency domain analyses assuming rightward harmonic pulses propagating in an infinite bar. Domain Ω (see Figure 11) is divided into two subdomains Ω^{PD} and Ω^{cont}, with $\Omega^{PD} \cup \Omega^{cont} = \Omega$ and $\Omega^{PD} \cap \Omega^{cont} = \Omega^{coupl}$. The classical theory of elasticity will be used in to describe the behaviour of the Ω^{cont} domain, whereas the linearized bond-based PD theory will be used for Ω^{PD}. Depending on the coupling approach, the coupling domain Ω^{coupl} can contain a single material position or an overlapping length. The PD theory is used in the middle of the bar with $\Omega^{PD} = [-l, l]$, whereas the rest of the bar is modelled using continuum elasticity with $\Omega^{cont} = \Omega^{cont,1} \cup \Omega^{cont,2} = (-\infty, -l] \cup [l, +\infty)$.

The incident pulse propagates from $-\infty$ toward ∞. Hence, in $\Omega^{cont,1}$, there are two pulses, ie, the initial incident pulse and the reflection from the first interface. In $\Omega^{cont,2}$, on the other hand, only the finally transmitted pulse exists. Denoting with $\boldsymbol{u}_R$, $\boldsymbol{u}_T$, and $\boldsymbol{d}$ the displacement fields in $\Omega^{cont,1}$, $\Omega^{cont,2}$, and Ω^{PD}, respectively, we assume solutions in the form $\boldsymbol{u}_R = U_R e^{-i\omega t}$, $\boldsymbol{u}_T = U_T e^{-i\omega t}$, and $\boldsymbol{d} = D e^{-i\omega t}$, and the governing equations become
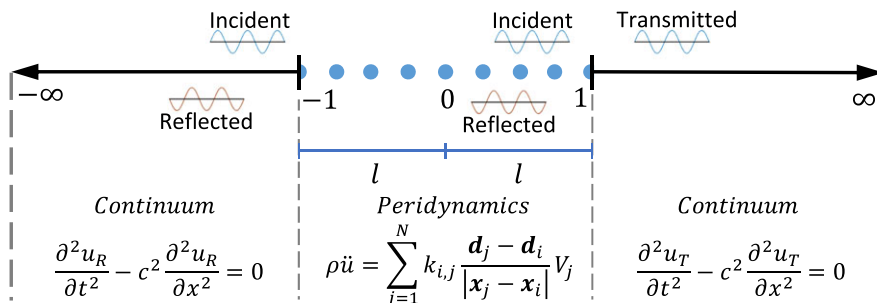
FIGURE 11 Continuum-PD coupling in an infinite 1D bar using a discrete interface. PD, peridynamic [Colour figure can be viewed at wileyonlinelibrary.com]

$$c^2 \frac{d^2 U_R}{dx^2} + \omega^2 U_R = 0 \qquad (40a)$$

$$-\omega^2 m_i D_i = \sum k \frac{D_j - D_i}{|x_j - x_i|} V_j V_i \qquad (40b)$$

$$c^2 \frac{d^2 U_T}{dx^2} + \omega^2 U_T = 0, \qquad (40c)$$

where U_R and U_T are solutions in the form

$$U_R = e^{i\kappa x} + R e^{-i\kappa x} \text{ and} \qquad (41a)$$

$$U_T = T e^{i\kappa x}, \qquad (41b)$$

with R and T being the reflection and transmission coefficients, respectively.[53] Energy conservation implies that $E_R + E_T = 1$, where $E_R = |R|^2$ is the reflected energy and $E_T = |T|^2$ is the transmitted energy. Using these definitions, the ability of a pulse to be transmitted across a coupling interface is evaluated.

Realisation of the first and second coupling case for the coupling of the discretized PD equation of motion with the continuum solution is carried out following the procedure presented in Sections 3.1 and 3.2, respectively. The first case requires the position of PD particles at the interface positions $x_1 = -l$ and $x_n = l$, where n is the total number of PD particles. Continuity and force equilibrium requirements are enforced at the interface positions resulting in the following equations:

$$U_R(-l) = D_1 \rightarrow D_1 = e^{-i\kappa l} + R e^{i\kappa l} \qquad (42a)$$

$$U_T(l) = D_n \rightarrow D_n = T e^{i\kappa l} \qquad (42b)$$

$$\Sigma F(-l) = 0 \qquad (42c)$$

$$\Sigma F(l) = 0. \qquad (42d)$$

Using as an example the case where $\delta = 2\Delta x$, Equations (42c) and (42d) become

$$\left(k_{1,2} + k_{1,3} \right) D_1 - k_{1,2} D_2 - k_{1,3} D_3 - EAi\kappa e^{i\kappa l} R = -EAi\kappa e^{-i\kappa l} \qquad (43a)$$

$$-k_{n,n-1} D_{n-1} - k_{n,n-2} D_{n-2} + \left(k_{n,n-1} + k_{n,n-2} \right) D_n - EAi\kappa e^{i\kappa l} T = 0, \qquad (43b)$$

where, earlier, $D_1, D_2, D_3, D_{n-2}, D_{n-1}$, and D_n are the particle displacements corresponding to the particles with positions $x = -l, -l + \Delta x, -l + 2\Delta x, l - 2\Delta x, l - \Delta x$, and l, respectively. Combining Equations (40a) to (40c), (41a) and (41b), (42a) to (42d), and (43a) and (43b), the system of equations can be solved for the R and T coefficients.

In the same manner, the system of equations for the second coupling case can be constructed. Without loss of generality, the example $\delta = 2\Delta x$ is implemented leading to the introduction of two ghost particles at each side of the PD domain. The continuity and force equilibrium requirements lead now to the following equations:

$$U_R\left(x_{g1}\right) = D_1 \rightarrow D_1 = e^{i\kappa x_{g1}} + R e^{-i\kappa x_{g1}} \qquad (44a)$$

$$U_R\left(x_{g2}\right) = D_2 \rightarrow D_2 = e^{i\kappa x_{g2}} + R e^{-i\kappa x_{g2}} \qquad (44b)$$

$$U_T\left(x_{g3}\right) = D_{n-1} \rightarrow D_{n-1} = T e^{i\kappa x_{g3}} \qquad (44c)$$

$$U_T\left(x_{g4}\right) = D_n \rightarrow D_n = T e^{i\kappa x_{g4}} \qquad (44d)$$

$$\Sigma F(-l) = 0 \qquad (44e)$$

$$\Sigma F(l) = 0, \qquad (44f)$$

where x_{g1}, x_{g2}, x_{g3} and x_{g4} are the positions of the ghost particles corresponding to the locations $x = -l - \Delta x/2, -l - 3\Delta x/2, l + \Delta x/2$, and $l+3\Delta x/2$, respectively. Although the force equilibrium of the second coupling case, described in Equations (44e) to (44f), looks similar to that of the first coupling case, described in Equations (42c) to (42d), it correlates the sum of the internal forces of each bond that crosses the interface with the internal forces from elasticity. For the example considered here, Equations (44e) to (44f) are expressed as follows:

$$k_{1,3} D_1 + \left(k_{2,3} + k_{2,4} \right) D_2 - \left(k_{1,3} + k_{2,3} \right) D_3 - k_{2,4} D_4 - i\kappa EA e^{i\kappa l} R = -i\kappa EA e^{-i\kappa l} \qquad (45a)$$

$$-k_{n-1,n-3} D_{n-3} - \left(k_{n-1,n-2} + k_{n,n-2} \right) D_{n-2} + \left(k_{n-1,n-2} + k_{n-1,n-3} \right) D_{n-1} + k_{n,n-2} D_n - i\kappa EA e^{i\kappa l} T = 0. \qquad (45b)$$

Finally, combining Equations (40a) to (40c), (41a) and (41b), (44a) to (44f), and (45a) and (45b), the R and T coefficients are computed for the second coupling case.
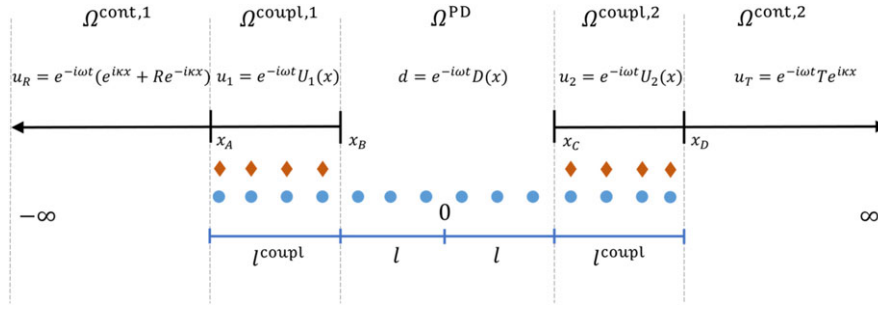
FIGURE 12 Illustration of continuum to peridynamic coupling using the third approach. Circles indicate the peridynamic particles, diamonds the Lagrange multipliers, and solid line the continuum bar [Colour figure can be viewed at wileyonlinelibrary.com]

For the third coupling case to be implemented, Ω^{PD} is extended within $\Omega^{cont,1}$ and $\Omega^{cont,2}$ by a length $l^{coupl} = x_B - x_A = x_D - x_C$ to create the overlapping regions $\Omega^{coupl,1}$ and $\Omega^{coupl,2}$, over which the coupling scheme is enforced (Figure 12). The assumption of solutions in the form given by Equations (41a) and (41b) is no longer valid within these domains. Assuming a linear blending function $a(x) = 1 - (x - x_A)/l^{coupl}$, an analytical derivation of the unknown fields $U_1(\boldsymbol{x})$ and $U_2(\boldsymbol{x})$ is sought. Using Equation (30a) and substituting $u_1 = e^{-i\omega t}U_1(\boldsymbol{x})$ in $\Omega^{coupl,1}$, the following differential equation is written:

$$a(x)U_{1,xx} + a(x)_{,x}U_{1,x} + \frac{\omega^2 \rho}{E}a(x)U_1 = \sum_{j=1}^{n} \frac{\Lambda_j}{EA}\delta\left(x - x_{\lambda_j}\right), x_A \leq \boldsymbol{x} \leq x_B, \tag{46}$$

where $\delta(\cdot)$ is the Dirac delta function. A solution in the form $\lambda_j = e^{i\omega t}\Lambda_j(x)$ was assumed for the Lagrange multipliers and n and x_{λ_j} are the total number and the positions of the Lagrange multipliers. A similar equation can be written for $\Omega^{coupl,2}$.

Using the change of variables $z = a(x)$, Equation (46) becomes

$$zU_{1,zz} + U_{1,z} + b_1^2 z U_1 = \sum_{j=1}^{n} b_2 \Lambda_j \delta\left(z - \widehat{x_{\lambda_j}}\right), 0 \leq z \leq 1, \tag{47}$$

where $b_1 = \sqrt{\rho\omega^2 l^2/E}$ and $b_2 = l/EA$ are two constants and $\widehat{x_{\lambda_j}} = \left(l^{coupl} + x_A - x_{\lambda_j}\right)/l^{coupl}$. This differential equation can be solved using the Hankel transform.[54,55] The solution obtained in $\Omega^{coupl,1}$ is given as follows:

$$U_1 = C_1 J_0(b_1 z) + C_2 Y_0(b_1 z) + \sum_{j=1}^{n} \frac{\pi}{2}b_2 \Lambda_j H\left(z - \widehat{x_{\lambda_j}}\right)\left(J_0\left(b_1\widehat{x_{\lambda_j}}\right)Y_0(b_1 z) - J_0(b_1 z)Y_0\left(b_1\widehat{x_{\lambda_j}}\right)\right), \tag{48}$$

where C_1 and C_2 are two constants, J_k and Y_k are the Bessel functions of the first and second kind with order k, and $H(\cdot)$ is the Heaviside function. As can be seen from Equation (48), as $z \to 0$ (ie, $x \to x_B$), $U_1 = C_1 J_0(0) + C_2 Y_0(0) \to -\infty$. This solution is not accepted as a finite result is expected and hence $C_2 = 0$.

On the interface between $\Omega^{coupl,1}$ and $\Omega^{cont,1}$, continuity and equilibrium conditions need to be satisfied. This leads to the following two equations:

$$U_R|_{x=x_A} = U_1|_{x=x_A} \to Re^{-i\kappa x_A} - C_1 J_0(b_1)$$
$$- \sum_{j=1}^{n} \frac{\pi}{2}b_2\Lambda_j\left(J_0\left(b_1\widehat{x_{\lambda_j}}\right)Y_0(b_1) - J_0(b_1)Y_0\left(b_1\widehat{x_{\lambda_j}}\right)\right) = -e^{i\kappa x_A} \tag{49}$$

and

$$\left.\frac{dU_R}{dx}\right|_{x=x_A} = \left.\frac{dU_1}{dx}\right|_{x=x_A} \to i\kappa Re^{-i\kappa x_A} + C_1\frac{b_1 J_0(b_1)}{l^{coupl}}$$
$$- \sum_{j=1}^{n} \frac{\pi b_2 b_1}{2l^{coupl}}\Lambda_j\left(J_1(b_1)Y_0\left(b_1\widehat{x_{\lambda_j}}\right) - J_0\left(b_1\widehat{x_{\lambda_j}}\right)Y_1(b_1)\right) = i\kappa e^{i\kappa x_A}. \tag{50}$$

Similarly, the same procedure can be repeated in $\Omega^{coupl,2}$ to relate the transmission coefficient T with the solution U_2. Using Equations (30b) and (30c), (49), and (50), the system of equations can be solved to compute the reflected and transmitted energy across the different domains.

The accuracy of the third coupling approach can be improved using a cubic (Hermitian) blending function with $a(x) = 1 - 3\left(\frac{x-x_A}{l^{coupl}}\right)^2 + 2\left(\frac{x-x_A}{l^{coupl}}\right)^3$ in Equation (46). In this case, the unknown displacement fields are approximated numerically
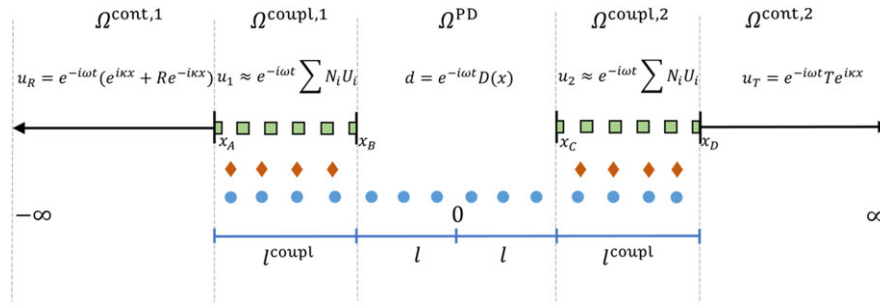
FIGURE 13　Third coupling case with finite elements in the coupling zone connected with continuum [Colour figure can be viewed at wileyonlinelibrary.com]
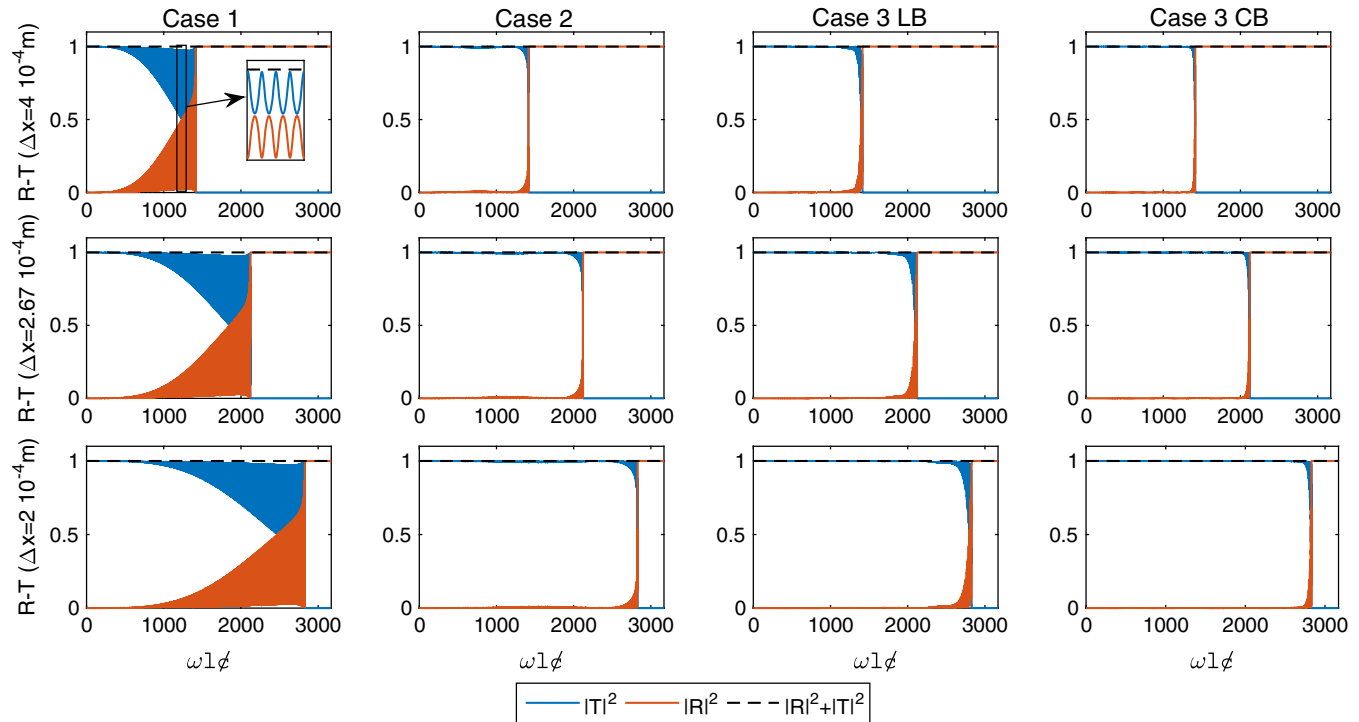
FIGURE 14　Reflection – Transmission diagrams for coupling cases 1, 2, 3 with a linear blending function (LB) and 3 with a cubic blending function (CB). The PD horizon was set to $\delta = 2\Delta x^{PD}$. Each row corresponds to a different PD discretization Δx^{PD} [Colour figure can be viewed at wileyonlinelibrary.com]

through FEs in $\Omega^{coupl,1}$ and $\Omega^{coupl,2}$. The FEs are coupled on one end with continuum using the first coupling approach and at the other end with PD using the third coupling approach (Figure 13). To avoid interference in the final $R - T$ diagrams due to the connection of the FE with the continuum, an extremely fine FE mesh was used, with $\Delta x^{FE} = 2 \times 10^{-5}$ m, to approximate as closely as possible the continuum case. For the solution of this configuration, Equations (32a) to (32c) are implemented in the frequency domain with the addition of continuity and force balance conditions, using Equations (42a) to (42d), respectively, between the FEs and the continuum at positions x_A and x_D.

Using the same model parameters as in the time-domain analyses (ie, $E = 200$ GPa, $A = 10^{-6}$ m^2, $\rho = 7850$ kg/m^3, and $l = 0.2$ m as the half-length of the PD domain), the transmission and reflection coefficients were computed with ω ranging from 0 to 4×10^7 rad/s for various values of Δx^{PD} and $\delta = n\Delta x^{PD}$. In Figure 14, Reflection – Transmission diagrams are reported for all coupling cases considered, for different PD discretization length Δx^{PD} values, whilst keeping the PD horizon constant $\delta = 2\Delta x^{PD}$. Red lines indicate the part of the initial energy that was reflected ($|R|^2$), whereas blue lines indicate the transmitted energy ($|T|^2$). Similarly, in Figure 15, the PD discretization length is kept constant, with $\Delta x^{PD} = 2 \times 10^{-4}$ m, and different values are used for the PD horizon. In all cases, energy conservation is satisfied. Results are presented in a nondimensional form with respect to the wave speed c and the length of Ω^{PD}, $2l = 0.4$ m.
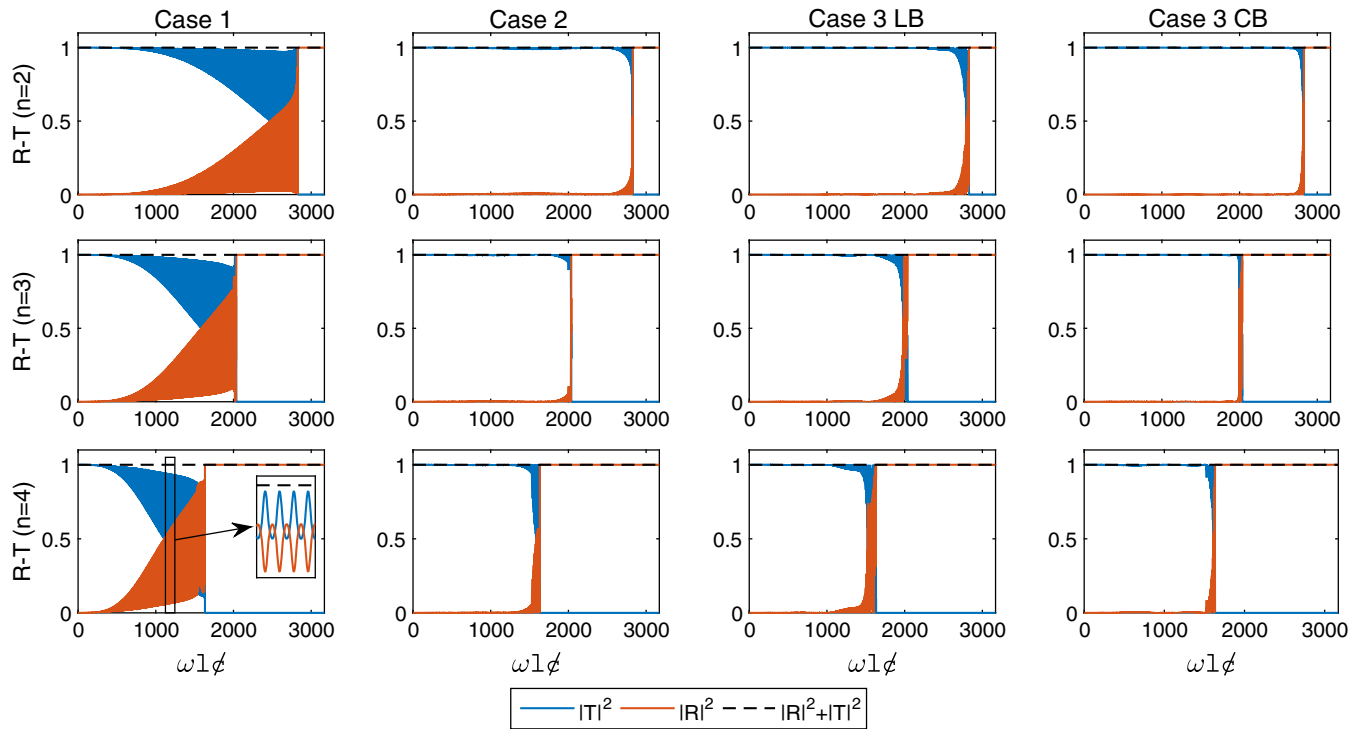
FIGURE 15 Reflection – Transmission diagrams for coupling cases 1, 2, 3 with a linear blending function (LB) and 3 with a cubic blending function (CB). The PD discretization was set to $\Delta x^{\mathrm{PD}} = 2 \times 10^{-4}$ m. Each row corresponds to a PD horizon value given as $\delta = n\Delta x^{\mathrm{PD}}$ [Colour figure can be viewed at wileyonlinelibrary.com]

All coupling approaches considered can achieve accurate wave propagation with minimal reflections for relatively small values of ω, as $|R|^2$ is close to 0 and $|T|^2 = 1$. As the frequency increases, the accuracy of the coupling deteriorates. When the forcing frequency of the pulse is close to or exceeds the cut-off frequency total reflection occurs and the transmitted energy vanishes. The PD discretization length Δx^{PD} implemented in Figure 15 is the same as that in Figure 10. For all cases, total reflection occurs at the frequency value predicted from the PD dispersion curve regardless of the coupling method chosen. Furthermore, the influence of Δx^{PD} and δ on the model's cut-off frequency is illustrated.

It is evident that, as the frequency of the input pulse approaches the model's cut-off frequency, the accuracy of the first coupling case deteriorates faster compared to the other methods. This means that further refinement is required to minimise the spurious reflections at the interface. The values of the reflected $|R|^2$ and transmitted energy $|T|^2$ oscillate till the cut-off frequency where total reflection occurs. Close-ups illustrating this fluctuation are provided in both Figure 14 and Figure 15. In this zone, the transmission coefficient is high for certain frequencies indicating that, if the problem solved contains monochromatic incident pulses, the method could be tailored to allow for accurate transmission. However, if the incident pulse excites a broad range of frequencies, only the frequencies corresponding to peaks will transmit. Using the other coupling cases, this zone is much smaller and restricted very close to the cut-off frequency, allowing to accurately simulate wave propagation with coarser grids for the same frequencies.

Using the results reported in Figure 14 and Figure 15, the third coupling case with the cubic blending function leads to the best results, followed by the second coupling case. Through these numerical tests, the improvement of implementing a cubic blending function within the formulation of the third coupling case is also highlighted as the coupling remains accurate for values closer to the cut-off frequency. It is noted here that, for the results presented, the overlapping length was set to $l^{\mathrm{coupl}} = 10\Delta x$. The coupling could be further improved by increasing the overlapping length, as illustrated in Figure 16. The accuracy of the coupling is improved, even for frequencies very close to the cut-off frequency with additional computational cost though.

Finally, of major importance is the implementation of the surface correction factor (Figure 17). The third coupling case is less affected from the skin effect, which appears at the particles near the boundary of Ω^{PD}, where the value of the blending function is almost zero (ie, energy has been transferred to Ω^{cont}). The first two coupling approaches are affected though, as the coupling interface is located near the area where the skin effect manifests. Comparing Figure 17 with the
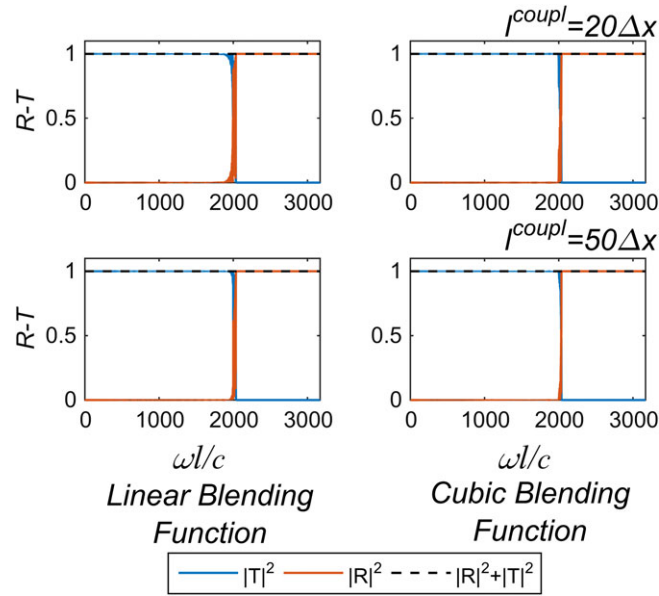
FIGURE 16 Influence of the overlapping length l^{coupl} when the third coupling approach is used with either the linear or the cubic blending function. The PD discretization and horizon values were set to $\Delta x^{PD} = 2 \times 10^{-4}$m and $\delta = 3\Delta x^{PD}$ [Colour figure can be viewed at wileyonlinelibrary.com]
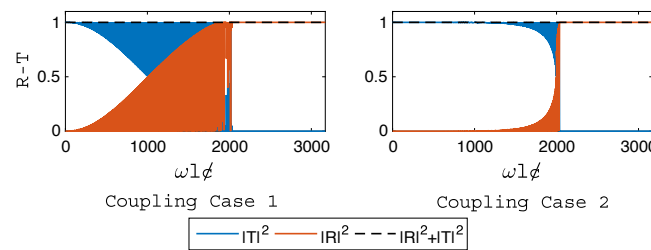
FIGURE 17 Influence of the surface correction for coupling cases 1 and 2 with $\Delta x^{PD} = 2 \times 10^{-4}$m and $\delta = 3\Delta x^{PD}$ [Colour figure can be viewed at wileyonlinelibrary.com]

corresponding diagrams from Figure 15, the accuracy of the coupling is affected significantly if appropriate correction is not implemented.

The third coupling case can lead to the most accurate coupling between PD and continua, given that an appropriate blending function and an adequately large overlapping region are provided. This increases the computational burden of the method and creates ambiguities on the a priori selection of blending functions in 2D and 3D problems. On the other hand, coupling approaches similar to the second coupling case or the method presented in the work of Zaccariotto et al[7] achieve comparable accuracy with lower cost and are easier to implement. The simplistic coupling presented in the first method should be avoided not only because it leads to strong reflections for relatively small frequencies but also because it requires conforming meshes that are problematic in problems involving higher dimensions.

6 ⎪ EXTENSION OF THE SECOND COUPLING CASE TO 2D PROBLEMS

The second coupling case is extended to 2D problems to further illustrate the importance of considering the cut-off frequencies of both the PD and FE models when addressing dynamic problems. The only thing that differs in the formulation of the second coupling case is the computation of the forces applied on the interface. In the 1D bar example, the computation of PD interfacial forces required to simply identify which bonds cross the interface (ie, bonds that connect a ghost and a normal particle) and what is the total force of these bonds. In 2D, the interface between the two descriptions is no longer a point but a line and thus it is necessary to compute the exact location where each bond crosses the interface. This is the location where PD forces are applied on the interface. In the following examples, linearized PD are coupled with four-node linear elasticity FE.
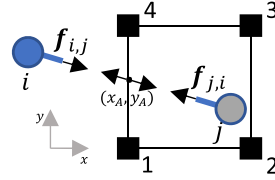
FIGURE 18 Extension of the second coupling case to 2D problems [Colour figure can be viewed at wileyonlinelibrary.com]

Assume that nodes 1 and 4, illustrated in Figure 18, define the PD-FE interface and particle j is a ghost particle. From the definition of linearized PD, the bond forces, with respect to the global axes, between particles i and j are computed as follows:

$$\boldsymbol{f} = \boldsymbol{R}^T \boldsymbol{K} \boldsymbol{R} \boldsymbol{d}, \tag{51}$$

where $\boldsymbol{f} = \{f_{i,j,x}\ f_{i,j,y}\ f_{j,i,x}\ f_{j,i,y}\}^T$ is the forcing vector, $\boldsymbol{d} = \{d_{i,x}\ d_{i,y}\ d_{j,x}\ d_{j,y}\}^T$ is the vector containing the displacements of particles i and j, $\boldsymbol{R}$ is the transformation matrix, and $\boldsymbol{K}$ is the local stiffness matrix in 2D given as follows:

$$\boldsymbol{K} = k_{i,j}^{\text{bond}} \begin{bmatrix} 1 & 0 & -1 & 0 \\ 0 & 0 & 0 & 0 \\ -1 & 0 & 1 & 0 \\ 0 & 0 & 0 & 0 \end{bmatrix}. \tag{52}$$

The value $k_{i,j}^{\text{bond}}$ is computed using Equation (22). From Equation (8), it is implied that $\boldsymbol{f}_{i,j}$ is equal and collinear to $\boldsymbol{f}_{j,i}$.

In 2D, it is convenient to treat the PD bond forces as externally applied forces to the FE that define the interface. Contrary to that, in the 1D case, the stiffness matrix of the coupled model was constructed directly in an explicit form by adding stiffness contributions. The force $\boldsymbol{f}_m^{\text{inter}} = -\boldsymbol{f}_{i,j} = \boldsymbol{f}_{j,i}$ is applied on the FE and it is concentrated at the intersection point (x_A, y_A) between the bond and the coupling interface and subscript m denotes the bond number. The point of application is defined using two Dirac delta functions. Assuming there are no other externally applied forces at the FE domain, then

$$\boldsymbol{F}^{\text{ext}} = \sum_{m=1}^{m_{tot}} \int \boldsymbol{N}^T \boldsymbol{f}_m^{\text{inter}} \delta(x - x_A) \delta(y - y_A) \, d\Gamma = \sum_{m=1}^{m_{tot}} \boldsymbol{N}_{x=x_A, y=y_A}^T \boldsymbol{f}_m^{\text{inter}}, \tag{53}$$

where N are the shape functions of the four-node element and m_{tot} is the total number of bonds that cross the coupling interface. Since the shape functions for nodes 2,3 vanish at the force application location, the interface force is effectively distributed between the two nodes that lie on the coupling interface. The final vector of external forces is computed by summing all the interface forces applied on the interface. Using matrix notation, the equation of motion in the FE domain can be written as follows:

$$\boldsymbol{M} \ddot{\boldsymbol{U}} + \boldsymbol{K}^{\text{FE}} \boldsymbol{U} = \boldsymbol{F}^{\text{ext}}. \tag{54}$$

The displacements of the ghost particles are again computed by interpolating the nodal displacements of their element using its shape functions as follows:

$$\boldsymbol{d}^{\text{ghost}} = \boldsymbol{N}^T \boldsymbol{U}. \tag{55}$$

The equation of motion for the particles in the PD domain is Equation (11). Now, the FE and PD equations are solved separately but are coupled together through Equation (55) and the external forcing in Equation (54). Time marching is performed again using the central difference method defined in Equations (16a) and (16b) and (17a) and (17b).

In the 1D problems, the bond constant $k(\xi)$ was assumed to be uniform within the PD horizon. For the 2D cases, a conical variation of the bond constant is implemented as it provides better convergence to classical elasticity.[40] Assuming plane stress conditions, the bond constant is expressed as follows:

$$k(\xi) = \left(1 - \frac{\xi}{\delta}\right) \frac{24E}{\pi \delta^3 (1 - v)}. \tag{56}$$

6.1 | Verification of the 2D model

To validate the coupling in 2D, a pulse propagating in a solid under plane stress conditions is considered. The boundary conditions and geometry are illustrated in Figure 19 (left). The length and the height of the plate are $L_x = 0.5$ m and $L_y = 0.25$ m, respectively, with a thickness of $t = 0.001$ m. The inner dimensions define the FE domain Ω^{FE} and are given
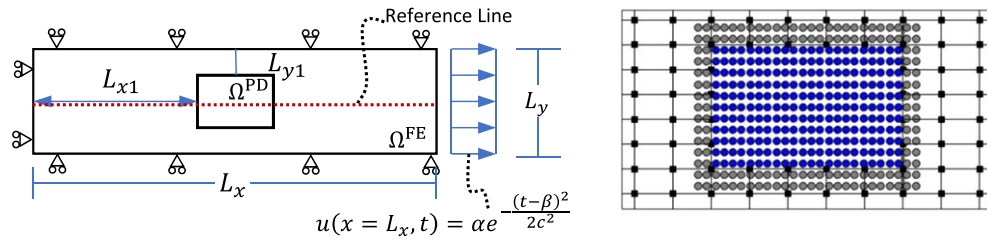
FIGURE 19 (left) Problem geometry and boundary conditions. (right) example of a coupled FE-PD model in 2D, black squares indicate FE nodes, blue circles PD particles and grey circles PD ghost particles [Colour figure can be viewed at wileyonlinelibrary.com]
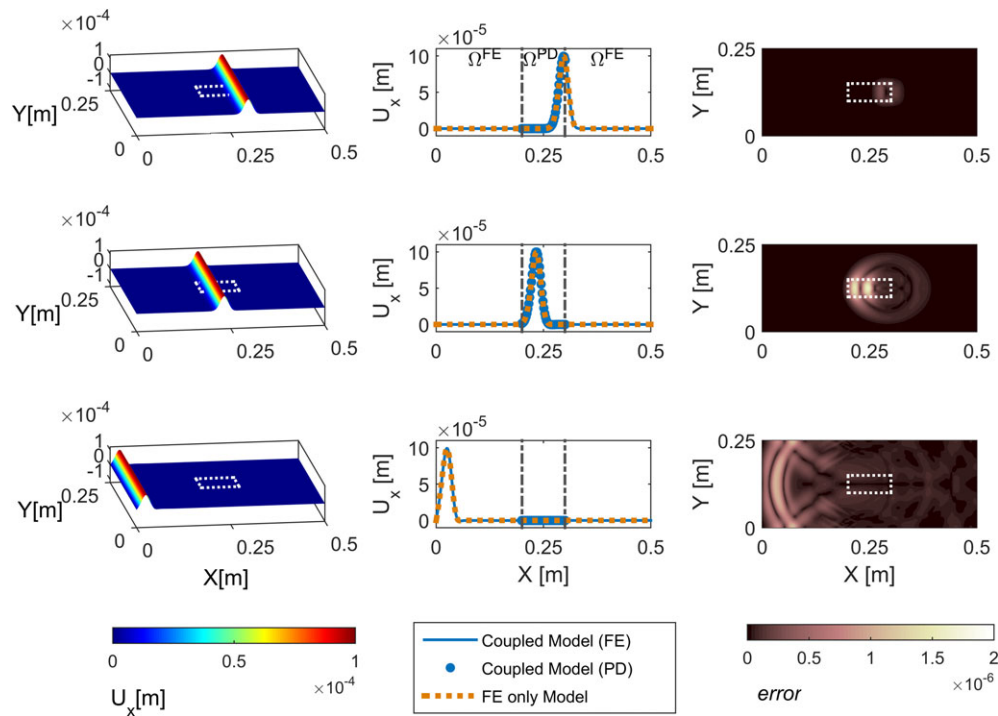
FIGURE 20 Comparison of the coupled model with FE solution at three different time steps. Left column: U_x displacements in the plate. White lines indicate the PD-FE interface. Middle column: Comparison of the U_x displacements along the reference line illustrated in Figure 19 with the FE solution. Right column: Plot of the error magnitude during each time step [Colour figure can be viewed at wileyonlinelibrary.com]

as $L_{x1} = 0.2$ m and $L_{y1} = 0.1$ m. Thus, the plate is modelled with FE apart from an area in the center, defining Ω^{PD}, which is modelled using PD. The time profile of the input pulse is Gaussian with $u(x = L_x, t) = ae^{-\frac{(t-\beta)^2}{2c^2}}$, $\alpha = 10^{-4}$ m, $\beta = 10^{-5}$ s, and $c = 2\,10^{-6}$ s. The y displacements are constrained at the top and bottom edges, whereas the x displacements are constrained at the left edge of the plate. The material is assumed elastic and isotropic with $E = 200$ GPa, $\nu = 1/3$, and $\rho = 7850$ kg/m^3.

The coupled problem was discretized with $\Delta x^{FE} = \Delta y^{FE} = 2 \times 10^{-3}$ m, and $\Delta x^{PD} = \Delta y^{PD} = 2.07 \times 10^{-4}$ m. The length of the PD horizon was set to $\delta = 5\Delta x^{PD}$. In total, 123 492 particles were used in the PD domain, out of which, 7330 where ghost particles. The FE element domain was discretized using 30 000 elements corresponding to 30 450 nodes. The total simulation time is $t_{tot} = 1 \times 10^{-4}$ s with steps $\Delta t = 5 \times 10^{-8}$ s. The standard FE solution was obtained using a uniform grid with $\Delta x^{FE} = \Delta y^{FE} = 2 \times$ m. In Figure 19 (right), an example of the discretization of Ω^{FE} and Ω^{PD} is illustrated. The location of the PD particles is independent of the FE nodal locations, thus simplifying the process. If the first coupling case was to be implemented, refinement of the FE mesh would be required near the interface for the FE nodes to coincide with the PD particles.

In the left column of Figure 20, the propagation of the Gaussian pulse is illustrated at time instants $t = 4.4 \times 10^{-5}$ s, $t = 5.7 \times 10^{-5}$ s, and $t = 9.9 \times 10^{-5}$ s. Similar to the 1D case, each time the pulse crosses a PD-FE interface, a reflection is generated. Since a much finer discretization was implemented in the PD domain compared to the FE domain, the cut-off frequency of the PD domain was higher than that of the FE domain, allowing the pulse to be transferred. This can also be seen in the middle column of Figure 20, where the displacements along the reference line, illustrated in Figure 19, are

compared for the coupled and the FE-only solutions. Compared to the amplitude of the pulse, the amplitude of spurious reflections is negligible, and the two solutions agree well. To further compare the two solutions, the L_2 norm of error is employed. Since the nodal points of the two solutions do not coincide in the Ω^{PD} region, the solution in the PD region is interpolated onto the FE nodal points through linear interpolation. The magnitude of error is defined as follows:

$$error = \left\| \boldsymbol{u}^{\text{FE only}} - \widehat{\boldsymbol{u}}^{\text{coupled}} \right\|_2, \tag{57}$$

where $\widehat{\boldsymbol{u}}^{\text{coupled}}$ contains the interpolated values of the coupled model $\boldsymbol{u}^{\text{coupled}}$ onto the FE nodes. The magnitude of the L_2 norm is plotted in the right column of Figure 20. As expected, discrepancies first appear when the pulse crosses for the first time the FE-PD interface and reach the maximum value of 2.02×10^{-6} when the pulse exits the PD domain. It is noted that the error here is not only due to the generated reflections but also due to differences in the numerical dispersion characteristics of the two solution methods. Still, the two solutions are in very good agreement in the whole computational domain.

6.2 | Partial trapping of pulses in PD-FE models

According to the findings of the 1D study, if the cut-off frequency of the PD domain in the previous example was not high enough to allow the pulse to be transmitted accurately, the spurious reflections generated would be more severe and affect the accuracy of the simulation. When coupling methods such as PDs with FE, it is desirable that the PD domain will be localised only in a small area of the computational domain, where steep stress gradients are expected. To accurately capture these phenomena, very fine discretization is usually required. It is thus expected that, in practical applications, the PD grid will be much finer than the FE mesh. Since the frequency content of the pulse was low enough to be transmitted within the coarse FE description, it was also able to propagate within the PD domain. In this case, consideration of the dispersion curves for each model is needed to make sure that the cut-off frequency of the FE domain is high enough to allow the pulse to be transmitted. At the same time, the cut-off frequency of the PD domain needs to be higher to reduce the spurious reflections due to the coupling. Consideration of the FE cut-off frequency is of equal importance to the PD one to achieve accurate coupling. This is evident in cases where the source of the pulse is located within the PD domain. One such case is considered in the next example.

Assuming an infinite plate with a hole at its center, the area around the hole is modelled with PD, whereas the rest of the plate with FE. To avoid interference due to the boundary conditions of the numerical model, the computational domain is truncated by adding a perfectly matched layer (PML) to attenuate outward travelling waves. In a recent study, unbounded problems were addressed using the PD differential operator and Sommerfeld boundary conditions.[56]

The PML was originally proposed by Berenger for applications in electromagnetic waves[57] and was later extended to applications involving elastic waves.[58] Here, the convolution PML (C-PML) proposed in the work of Matzen[59] for time-domain analyses is employed. In the PML region, the coordinate variables x_i, $i = 1,2$ of the problem are transformed into the stretched coordinate variables $\tilde{x}_i$, in each direction, given as[58,60]

$$\tilde{x}_i = \int_0^{x_i} s_i\,(x_i, \omega)\,dx_i, i = 1, 2, \tag{58}$$

where ω is the angular frequency and s_i are the stretched coordinate functions, proposed by Kuzuoglu and Mittra,[61] ie,

$$s_i\,(x_i\omega) = \kappa_i\,(x_i, \omega) + \frac{\beta_i\,(x_i)}{\alpha_i\,(x_i) + i\omega}. \tag{59}$$

Three coordinate-wise functions are introduced in Equation (59), $\beta_i(x_i) \geq 0$, $\kappa_i(x_i, \omega) \geq 1$, and $\alpha_i(x_i) \geq 0$. $\beta_i(x_i)$ controls the attenuation in the PML region, whereas $\kappa_i(x_i, \omega)$ and $\alpha_i(x_i)$ enhance the attenuation of evanescent waves. In the work of Matzen,[59] it was shown that, when near-grazing waves do not manifest, the selection $\kappa_i(x_i, \omega) = 1$ and $\alpha_i(x_i) = 0$ simplifies the PML computations as one of the convolution terms disappears without affecting significantly the accuracy. Since this is applicable to the case considered here, these values are adopted. The function $\beta_i(x_i)$ is defined in the works of Matzen[59] and Madsen et al[60] and the references therein as follows:

$$\beta_i\,(x_i) = \beta_i^{\max} \left(\frac{x_i - x_i^0}{2d_i} \right)^3, \tag{60}$$

where $\beta_i^{\max} = -\left(4c_p \log_{10} R_0\right) / (2d_i)$, $R_0 = 10^{-8}$ is the theoretical reflection coefficient at normal incidence, x_i^0 is the location of the PML interface, and d_i is the PML thickness in each direction.
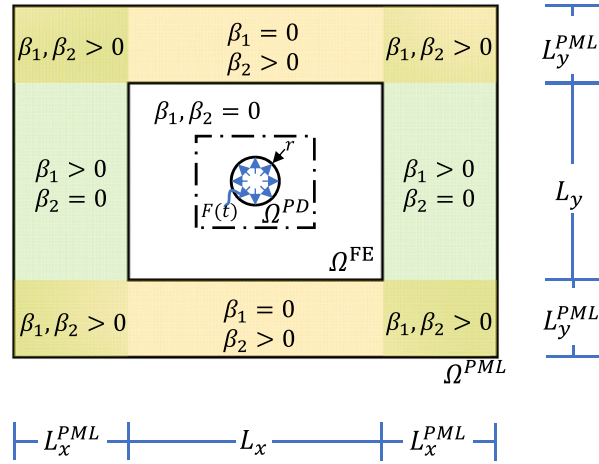
FIGURE 21 A PML layer is added around Ω^{FE}. Within the PML region the material becomes anisotropic and attenuates the outward going pulses [Colour figure can be viewed at wileyonlinelibrary.com]

TABLE 2 Summary of model parameters

Parameter	Value	Parameter	Value
$L_x = L_y$	0.5 m	t_{tot}	2×10^{-4} s
$L_{x1} = L_{y1}$	0.2 m	Δt	2×10^{-7} s
$L_x^{PML} = L_y^{PML}$	0.3 m	$\Delta x^{PD} = \Delta y^{PD}$	3.11×10^{-4} m
t	1 mm	$\Delta x^{PML} = \Delta y^{PML}$	9.37×10^{-4} m
r	3 mm	$\Delta x^{FE} = \Delta y^{FE}$ (fine)	13×10^{-4} m
E	200 GPa	$\Delta x^{FE} = \Delta y^{FE}$ (coarse)	33×10^{-4} m
v	1/3	$F_{\max}$	1.06×10^4 MPa
δ	$3\Delta x^{PD}$	ρ	7850 Kg/m^3

The coordinate stretching performed in the PML region leads to a nonhomogeneous differential operator. To extract the original one, artificial anisotropy is introduced to the material. The FE equation of motion now is

$$M\ddot{U} + Z\dot{U} + KU + g = F^{\text{ext}}, \tag{61}$$

where M, Z, K are the mass, damping, and stiffness matrices, and g is a convolution term defined in.[53] The interested reader can find more details in the work of Ben-Menahem and Singh[53] on the FE implementation of the PML, whereas a PML formulation for state-based PDs can be found in the work of Wildman and Gazonas.[62] The geometry of the problem is illustrated in Figure 21 along with the definition of the coordinate-wise function β_i in different areas of the plate. A radial pressure is applied at the walls of the hole with $F(t) = F_{\max} e^{-\frac{1}{2}\left(\frac{t-a_2}{a_3}\right)^2}$. The problem solution is repeated two times; the first time the FE discretization was refined to minimise the spurious reflections generated, whereas, for the second time, a coarser FE mesh was used. In both solutions, the PD and the FE discretizations in the PML were not changed. The model parameters are summarized in Table 2. The displacements are constrained on the outer perimeter of the PML as according to the work of Matzen,[59] this improves the stability during time marching.

The results using the coarser and finer discretization are illustrated in Figure 22 and Figure 23. The displacement magnitude $|U| = \sqrt{U_x^2 + U_y^2}$ is plotted at different time instants as the pulse propagates along the PD-FE and FE-PML interfaces till it is finally attenuated. In the same figures, the total energy in the PD and the FE model is also included. When the fine FE discretization is used, the pulse propagates without significant reflections across the PD-FE interface. The total energy provided into the PD model is transferred to the FE model and subsequently exits the domain (vanishes due to the introduction of the PML). On the other hand, when the coarse mesh is used, only part of the energy is transmitted to the FE domain, whereas approximately 16% of the energy is trapped within the PD domain.

By making the FE mesh coarser, the cut-off frequency is reduced, and significant spurious reflections are generated at the interface. These reflections are trapped in the PD domain and are unable to reach the PML region. In practice,
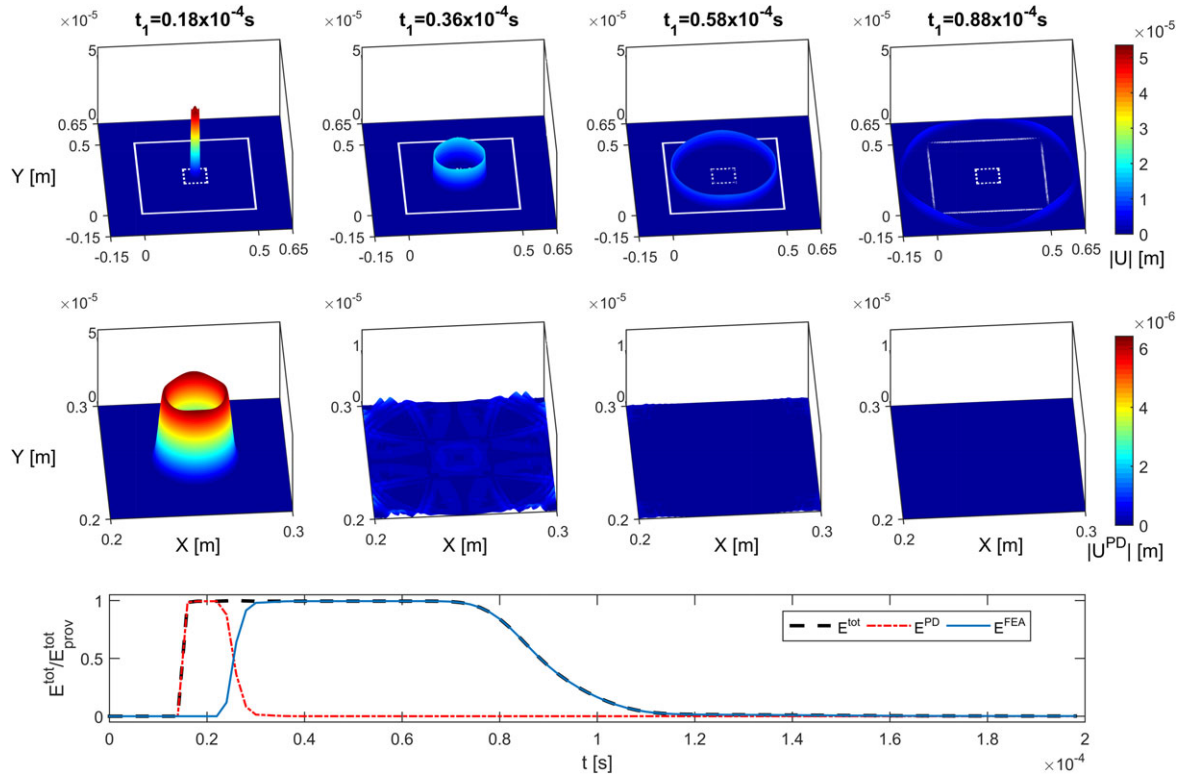
FIGURE 22 Pulse propagation with close up in Ω^{PD} and energy transferring using the fine FE mesh [Colour figure can be viewed at wileyonlinelibrary.com]
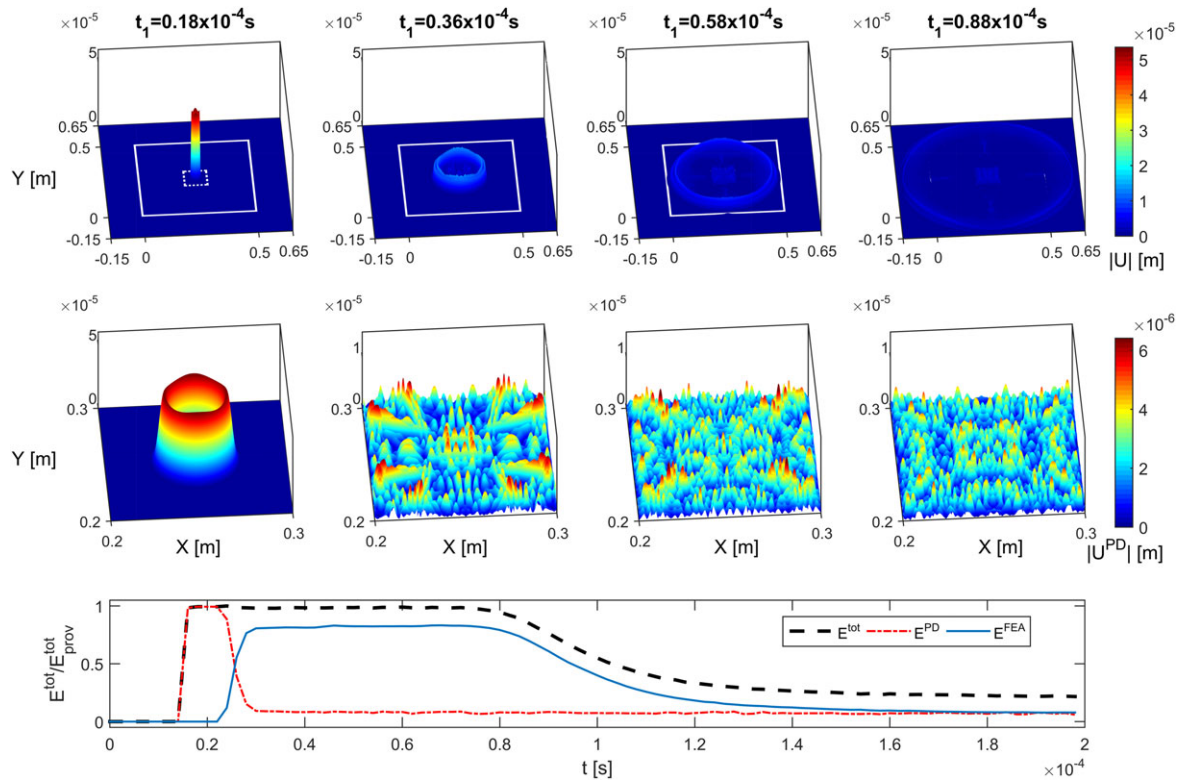
FIGURE 23 Pulse propagation with close up in Ω^{PD} and energy transferring using the coarse FE mesh. Approximately 16% of the total energy is trapped within the peridynamic domain [Colour figure can be viewed at wileyonlinelibrary.com]

if the frequency content of the propagating pulse is known beforehand, the discretization parameters of the numerical descriptions will be selected accordingly. However, application of impact-like loads in the PD domain will excite the whole frequency spectrum of the finer model. It is thus desired that the two models have similar cut-off frequencies to minimise the reflected energy. In problems involving dynamic crack propagation, mismatch between the two descriptions will lead to accumulation of the trapped energy within the PD domain that will lead to erroneous and unrealistic results.

7 | CONCLUSIONS

Three approaches to couple FE meshes with PD grids have been formulated to study the spurious reflections that appear during dynamic simulations. Although these reflections cannot be avoided completely, they can be minimised through careful selection of the model parameters. The first coupling approach presented is the simplest one and used mainly for comparison purposes. Its use is restrictive as it requires conforming meshes, posing difficulties for 2D and 3D applications.[14] The second and third approach can be extended to problems with higher dimensions more efficiently,[7,26,32,63] as both of them can couple models with no restrictions on the position of the PD particles and the FE nodes.

The coupling approaches were compared through numerical tests in a 1D bar for pulses with different shapes and frequency contents. Initially, the energy drift is computed in the time domain for incident pulses with modular and Gaussian shape. The numerical tests are then continued in the frequency domain where the discrete PD model is coupled with continuum mechanics. This allows to study more systematically the accuracy of each coupling approach by computing the transmission and the reflection coefficients in an infinite bar. The discretization size and the value of the PD horizon are of outmost importance toward an efficient coupling as they control the cut-off frequency of the numerical solution. The results indicate that the third coupling case with a cubic blending function leads to the most accurate energy transmission. Comparable accuracy can be achieved implementing the second coupling case (or similar methods presented in the literature, eg, the work of Zaccariotto et al[7]). This approach is simpler to formulate, less computationally expensive, and does not entail ambiguities with regards to the optimal selection and construction of blending functions.

The second coupling case is also extended to 2D problems to illustrate the significance of considering the cut-off frequencies of both the finer and the coarser models. An axially loaded hole in an infinite domain is used as an example. Analytical solutions of similar problems can be found in the work of Graff.[64] In dynamic problems, where the source of the pulse is located within the fine PD model (eg, dynamic crack propagation), entrapment of the energy can be observed. In such situations, cut-off frequency of the coarser model needs to be adjusted to match that of the finer model.

ORCID

Theodosios K. Papathanasiou 🆔 https://orcid.org/0000-0003-2130-5172

REFERENCES

1. Han F, Lubineau G, Azdoud Y. Adaptive coupling between damage mechanics and peridynamics: a route for objective simulation of material degradation up to complete failure. *J Mech Phys Solids*. 2016;94:453-472.
2. Bobaru F, Ha YD. Adaptive refinement and multiscale modeling in 2D peridynamics. *J Multiscale Comput Eng*. 2011;9:635-659.
3. Dipasquale D, Zaccariotto M, Galvanetto U. Crack propagation with adaptive grid refinement in 2D peridynamics. *Int J Fract*. 2014;190:1-22.
4. Fung Y, Tong P, Chen X. *Classical and Computational Solid Mechanics*. Singapore: World Scientific Publishing Company; 2017.
5. Silling SA, Askari E. A meshfree method based on the peridynamic model of solid mechanics. *Comput Struct*. 2005;83:1526-1535.
6. Kilic B, Madenci E. An adaptive dynamic relaxation method for quasi-static simulations using the peridynamic theory. *Theor Appl Fract Mech*. 2010;53:194-204.
7. Zaccariotto M, Mudric T, Tomasi D, Shojaei A, Galvanetto U. Coupling of FEM meshes with peridynamic grids. *Comput Methods Appl Mech Eng*. 2018;330:471-497.
8. Liu W, Hong J-W. A coupling approach of discretized peridynamics with finite element method. *Comput Methods Appl Mech Eng*. 2012;245-246:163-175.
9. Kilic B, Madenci E. Coupling of peridynamic theory and the finite element method. *J Mech Mater Struct*. 2010;5:707-733.
10. Zaccariotto M, Tomasi D, Galvanetto U. An enhanced coupling of PD grids to FE meshes. *Mech Res Commun*. 2017;84:125-135.
11. De Meo D, Zhu N, Oterkus E. Peridynamic modeling of granular fracture in polycrystalline materials. *J Eng Mater Technol*. 2016;138.

12. Horstemeyer MF. Multiscale modeling: a review. In: *Practical Aspects of Computational Chemistry: Methods, Concepts and Applications*. Dordrecht, The Netherlands: Springer Science+Business Media; 2010:87-135.

13. Miller RE, Tadmor EB. A unified framework and performance benchmark of fourteen multiscale atomistic/continuum coupling methods. *Model Simul Mater Sci Eng*. 2009;17:053001.

14. Fish J. *Multiscale Methods: Bridging the Scales in Science and Engineering*. Oxford, UK: Oxford University Press; 2010.

15. Talebi H, Silani M, Bordas SP, Kerfriden P, Rabczuk T. A computational library for multiscale modeling of material failure. *Computational Mechanics*. 2014;53:1047-1071.

16. Aubertin P, Réthoré J, De Borst R. Energy conservation of atomistic/continuum coupling. *Int J Numer Methods Eng*. 2009;78:1365-1386.

17. Xu M, Belytschko T. Conservation properties of the bridging domain method for coupled molecular/continuum dynamics. *Int J Numer Methods Eng*. 2008;76:278-294.

18. Faucher V, Combescure A. A time and space mortar method for coupling linear modal subdomains and non-linear subdomains in explicit structural dynamics. *Comput Methods Appl Mech Eng*. 2003;192:509-533.

19. Herry B, Di Valentin L, Combescure A. An approach to the connection between subdomains with non-matching meshes for transient mechanical analysis. *Int J Numer Methods Eng*. 2002;55:973-1003.

20. Seleson P, Beneddine S, Prudhomme S. A force-based coupling scheme for peridynamics and classical elasticity. *Comput Mater Sci*. 2013;66:34-49.

21. Madenci E, Oterkus E. *Peridynamic Theory and Its Applications*. New York, NY: Springer Science+Business Media; 2014.

22. Han F, Lubineau G. Coupling of nonlocal and local continuum models by the Arlequin approach. *Int J Numer Methods Eng*. 2012;89:671-685.

23. Dhia HB, Rateau G. The Arlequin method as a flexible engineering design tool. *Int J Numer Methods Eng*. 2005;62:1442-1462.

24. Di Paola M, Failla G, Zingales M. The mechanically-based approach to 3D non-local linear elasticity theory: long-range central interactions. *Int J Solids Struct*. 2010;47:2347-2358.

25. Lubineau G, Azdoud Y, Han F, Rey C, Askari A. A morphing strategy to couple non-local to local continuum mechanics. *J Mech Phys Solids*. 2012;60:1088-1102.

26. Galvanetto U, Mudric T, Shojaei A, Zaccariotto M. An effective way to couple FEM meshes and peridynamics grids for the solution of static equilibrium problems. *Mech Res Commun*. 2016;76:41-47.

27. Mossaiby F, Shojaei A, Zaccariotto M, Galvanetto U. OpenCL implementation of a high performance 3D peridynamic model on graphics accelerators. *Comput Math Appl*. 2017;74:1856-1870.

28. Silling SA. Reformulation of elasticity theory for discontinuities and long-range forces. *J Mech Phys Solids*. 2000;48:175-209.

29. Emmrich E, Weckner O. The peridynamic equation of motion in non-local elasticity theory. Paper presented at: III European Conference on Computational Mechanics: Solids, Structures and Coupled Problems in Engineering; 2006; Lisbon, Portugal.

30. Askari E, Bobaru F, Lehoucq RB, Parks ML, Silling SA, Weckner O. Peridynamics for multiscale materials modeling. *J Phys: Conf Ser*. 2008;125:012078.

31. Oterkus S, Madenci E, Agwai A. Fully coupled peridynamic thermomechanics. *J Mech Phys Solids*. 2014;64:1-23.

32. Bobaru F, Foster JT, Geubelle PH, Silling SA. *Handbook of Peridynamic Modeling*. Boca Raton, FL: CRC Press; 2017.

33. Giannakeas IN, Papathanasiou TK, Bahai H. Simulation of thermal shock cracking in ceramics using bond-based peridynamics and FEM. *J Eur Ceram Soc*. 2018;38:3037-3048.

34. Bobaru F, Yang M, Alves LF, Silling SA, Askari E, Xu J. Convergence, adaptive refinement, and scaling in 1D peridynamics. *Int J Numer Methods Eng*. 2009;77:852-877.

35. Ha YD, Bobaru F. Characteristics of dynamic brittle fracture captured with peridynamics. *Eng Fract Mech*. 2011;78:1156-1168.

36. Liu W, Hong JW. Discretized peridynamics for linear elastic solids. *Computational Mechanics*. 2012;50:579-590.

37. Silling SA, Bobaru F. Peridynamic modeling of membranes and fibers. *Int J Non-Linear Mech*. 2005;40:395-409.

38. Zaccariotto M, Luongo F, Sarego G, Galvanetto F. Examples of applications of the peridynamic theory to the solution of static equilibrium problems. *Aeronaut J*. 2015;119:677-700.

39. Littlewood DJ. *Roadmap for Peridynamic Software Implementation*. Sandia report. Livermore, CA: Sandia National Laboratories; 2015.

40. Ha YD, Bobaru F. Studies of dynamic crack propagation and crack branching with peridynamics. *Int J Fract*. 2010;162:229-244.

41. Chopra AK. *Dynamics of Structures: Theory and Applications to Earthquake Engineering*. Englewood Cliffs, NJ: Prentice Hall; 1995.

42. Gerstle W, Sau N, Silling S. Peridynamic modeling of concrete structures. *Nucl Eng Des*. 2007;237:1250-1258.

43. Xiao S, Belytschko T. A bridging domain method for coupling continua with molecular dynamics. *Comput Methods Appl Mech Eng*. 2004;193:1645-1669.

44. Guidault P, Belytschko T. On the L^2 and the H^1 couplings for an overlapping domain decomposition method using Lagrange multipliers. *Int J Numer Methods Eng*. 2007;70:322-350.

45. Bauman PT, Dhia HB, Elkhodja N, Oden JT, Prudhomme S. On the application of the Arlequin method to the coupling of particle and continuum models. *Computational Mechanics*. 2008;42:511-530.

46. Bobaru F, Hu W. The meaning, selection, and use of the peridynamic horizon and its relation to crack branching in brittle materials. *Int J Fract*. 2012;176:215-222.

47. Fackeldey K. Challenges in atomistic-to-continuum coupling. *Math Probl Eng*. 2015;2015.

48. Silling SA, Zimmermann M, Abeyaratne R. Deformation of a peridynamic bar. *J Elast*. 2003;73:173-190.

49. Dayal K. Leading-order nonlocal kinetic energy in peridynamics for consistent energetics and wave dispersion. *J Mech Phys Solids.* 2017;105:235-253.

50. Mikata Y. Analytical solutions of peristatic and peridynamic problems for a 1D infinite rod. *Int J Solids Struct.* 2012;49:2887-2897.

51. Diyaroglu C, Oterkus E, Oterkus S, Madenci E. Peridynamics for bending of beams and plates with transverse shear deformation. *Int J Solids Struct.* 2015;69-70:152-168.

52. Butt SN, Timothy JJ, Meschke G. Wave dispersion and propagation in state-based peridynamics. *Computational Mechanics.* 2017;60:725-738.

53. Ben-Menahem A, Singh SJ. *Seismic Waves and Sources.* New York, NY: Springer-Verlag; 2012.

54. Zaitsev VF, Polyanin AD. *Handbook of Exact Solutions for Ordinary Differential Equations.* Boca Raton, FL: CRC Press; 2002.

55. Debnath L, Bhatta D. *Integral Transforms and Their Applications.* Boca Raton, FL: CRC Press; 2006.

56. Shojaei A, Galvanetto U, Rabczuk T, Jenabi A, Zaccariotto M. A generalized finite difference method based on the Peridynamic differential operator for the solution of problems in bounded and unbounded domains. *Comput Methods Appl Mech Eng.* 2019;343:100-126.

57. Berenger J-P. A perfectly matched layer for the absorption of electromagnetic waves. *J Comput Phys.* 1994;114:185-200.

58. Collino F, Tsogka C. Application of the perfectly matched absorbing layer model to the linear elastodynamic problem in anisotropic heterogeneous media. *Geophysics.* 2001;66:294-307.

59. Matzen R. An efficient finite element time-domain formulation for the elastic second-order wave equation: a non-split complex frequency shifted convolutional PML. *Int J Numer Methods Eng.* 2011;88:951-973.

60. Madsen SS, Krenk S, Hededal O. Perfectly matched layer (PML) for transient wave propagation in a moving frame of reference. Paper presented at: 4th International Conference on Computational Methods in Structural Dynamics and Earthquake Engineering; 2013; Kos Island, Greece.

61. Kuzuoglu M, Mittra R. Frequency dependence of the constitutive parameters of causal perfectly matched anisotropic absorbers. *IEEE Microw Guid Wave Lett.* 1996;6:447-449.

62. Wildman RA, Gazonas GA. A perfectly matched layer for peridynamics in two dimensions. *J Mech Mater Struct.* 2012;7:765-781.

63. Qiao H, Yang Q, Chen W, Zhang C. Implementation of the Arlequin method into ABAQUS: basic formulations and applications. *Adv Eng Softw.* 2011;42:197-207.

64. Graff KF. *Wave Motion in Elastic Solids.* Mineola, NY: Dover Publications; 2012.